BNL-97296-2012-JA

RMetS
Royal Meteorological Society

The role of precipitation size distributions in km-scale NWP simulations of intense precipitation: evaluation of cloud properties and surface precipitation

Kwinten Van Weverberg,[a,b]* Nicole P.M van Lipzig,[a] Laurent Delobbe[c] and Andrew M. Vogelmann[b]

[a]*Department of Earth and Environmental Sciences, K. U. Leuven, Heverlee, Belgium*
[b]*Atmospheric Sciences Division, Brookhaven National Laboratory, Upton, NY, USA*
[c]*Royal Meteorological Institute, Uccle, Belgium*

*Correspondence to: K. Van Weverberg, Brookhaven National Laboratory, Atmospheric Sciences Division, Brookhaven National Laboratory Building 490-D, Atmospheric Sciences Division, Upton, NY, USA.
E-mail: kvweverberg@bnl.gov

We investigate the sensitivity of simulated cloud properties and surface precipitation to assumptions regarding the size distributions of the precipitating hydrometeors in a one-moment bulk microphysics scheme. Three sensitivity experiments were applied to two composites of 15 convective and 15 frontal stratiform intense precipitation events observed in a coastal midlatitude region (Belgium), which were evaluated against satellite-retrieved cloud properties and radar-rain-gauge derived surface precipitation. It is found that the cloud optical thickness distribution was well captured by all experiments, although a significant underestimation of cloudiness occurred in the convective composite. The cloud-top-pressure distribution was improved most by more realistic snow size distributions (including a temperature-dependent intercept parameter and non-spherical snow for the calculation of the slope parameter), due to increased snow depositional growth at high altitudes. Surface precipitation was far less sensitive to whether graupel or hail was chosen as the rimed ice species, as compared to previous idealized experiments. This smaller difference in sensitivity could be explained by the stronger updraught velocities and higher freezing levels in the idealized experiments compared to typical coastal midlatitude environmental conditions. Copyright © 2012 Royal Meteorological Society

Key Words: microphysics parametrization; cloud optical thickness; satellite; radar

Received 17 August 2011; Revised 9 January 2012; Accepted 28 February 2012; Published online in Wiley Online Library

Citation: Van Weverberg K, van Lipzig NPM, Delobbe L, Vogelmann AM. 2012. The role of precipitation size distributions in km-scale NWP simulations of intense precipitation: evaluation of cloud properties and surface precipitation. *Q. J. R. Meteorol. Soc.* DOI:10.1002/qj.1933

1. Introduction

The parametrization of microphysical processes in numerical weather-prediction (NWP) models bears large importance for the correct simulation of clouds and surface precipitation. Typically, NWP models apply the conversion processes from excess water vapour to clouds and surface precipitation to the entire size distribution of a number of hydrometeor species (bulk microphysical models). This approach is more computationally efficient than applying those formulations to separate size bins of those species (i.e. bin or spectral microphysical models). In order to mimic the behaviour of the size distribution evolution, one or more moments of the distribution are related to the prognostic

variables in the model. One-moment schemes typically predict only the mixing ratio (given by the 3rd moment, e.g. Lin *et al.*, 1983; Rutledge and Hobbs, 1983; Kong and Yau, 1997), while two-moment schemes also predict the number concentration (given by the 0th moment, e.g. Ferrier, 1994; Morrison *et al.*, 2005; Seifert and Beheng, 2006).

Over the past decade or so, uncertainties in one-moment microphysical models have been shown to affect quantitative precipitation forecasts. For frontal stratiform precipitation events, surface precipitation was sensitive to the representation of the snow size distribution and fall velocity (Thompson *et al.*, 2004; Colle *et al.*, 2005; Serrafin and Ferretti, 2007; Woods *et al.*, 2007). For convective precipitation events, the size and nature of the largest rimed ice species (either hail or graupel) have been shown to have a significant impact on surface precipitation (Gilmore *et al.*, 2004; van den Heever and Cotton, 2004; Cohen and McCaul, 2006; Morrison and Milbrandt, 2011). In operational NWP, a single model set-up is required to satisfactorily simulate stratiform and convective precipitation events. In that context, it is important to understand how model modifications designed to improve moist processes under certain synoptic conditions affect the simulations during totally different synoptic conditions.

Most of the previously conducted studies were associated with single cases and, in the case of convection, often dealt with idealized model set-ups that neglected the influence of certain boundary-layer and radiative feedbacks. For example, Van Weverberg *et al.* (2011b) and Reinhardt and Seifert (2006) showed via observed cases of convection that the choice of graupel or hail was of much less importance to surface precipitation than was expected from idealized simulations. It is unknown why real-case simulations tend to show less sensitivity compared to idealized simulations. According to Van Weverberg *et al.* (2011b), this was due to different environmental conditions in the idealized and the real-case simulations, while Reinhardt and Seifert (2006) suggested this was due to more negative feedbacks in the real-case simulations, associated with longer integration times and the smaller importance of graupel (due to stratiform areas in between the convection). These issues need to be addressed to understand the extent to which the rimed ice sensitivities found in prior idealized studies can be generalized to other cases with various environmental characteristics.

Recently, the spatial and temporal coverage offered by satellite and radar data, along with the algorithms that retrieve cloud properties from these data, have significantly increased in quality and now enable quantitative comparison with simulated cloud and precipitation fields (van Lipzig *et al.*, 2006). Programmes are ongoing to optimize the use of existing instrumentation and create datasets of *in situ* and remote-sensing instruments with a special focus on water-cycle variables (Crewell *et al.*, 2008), which have proven to be valuable for evaluating the process chain from the water vapour distribution through cloud processes to the amount of precipitation reaching the ground (Böhme *et al.*, 2011; Van Weverberg *et al.*, 2011a; Akkermans *et al.*, 2012). Hence, it is increasingly useful to use such data and perform real-case simulations to understand how assumptions in the parametrizations affect the realistic simulation of clouds and precipitation.

This study examines the impact that assumptions regarding the size distributions of precipitating hydrometeors have on surface precipitation and cloud properties, and the extent to which the relationships found in previous studies can be generalized. Experiments have been designed to understand: (i) how the nature of snow and the rimed ice species affect moist processes under stratiform and convective conditions; (ii) how relevant idealized case-study sensitivities are to the NWP of observed intense convection; and (iii) how different model versions compare with recently available, high-resolution remotely sensed cloud properties. These properties include satellite-derived cloud optical thickness and cloud-top pressure, and quantitative information derived from radar using new techniques. To ensure relevance to the current NWP community, the sensitivity experiments were applied to simulations with a one-moment microphysics scheme and horizontal grid spacing of 3 km.

We adopted a composite approach, selecting a large number of observed intense precipitation events, which has the advantage of detecting and understanding model deficiencies and model sensitivities for a relatively homogeneous sample. Most studies have evaluated the representation of clouds and precipitation either by evaluation of long-term model integrations or by case-studies. The long-term model evaluation has the advantage of identifying systematic model behaviour, but it is often found difficult to understand the model behaviour. In case-studies, a detailed analysis and improved understanding of modelled processes is eased, but there is the risk of the case not being representative for the general model behaviour. By using the composite approach, advantages of both the long-term model evaluation and detailed case-studies can be fully exploited. The composite approach that we adopted is similar to the regime-dependent model evaluation (Jakob, 2003), where a multitude of cloud states observed in the atmosphere are stratified into recurring regimes.

The next section provides a description of the atmospheric model employed (2.1) and the sensitivity experiments performed (2.2). Subsection 2.3 describes details of the observational data used for comparison to the sensitivity experiments. Results and analysis are given in section 3, which are discussed and summarized in section 4.

2. Data and methods

2.1. *Model description*

The model employed here is the Advanced Regional Prediction System (ARPS), which is a non-hydrostatic mesoscale meteorological model developed at the University of Oklahoma (Xue *et al.*, 2000, 2001). The finite-difference equations of the model are discretized on an Arakawa C-grid, employing a terrain-following coordinate in the vertical direction. Advection is solved with a fourth-order central differencing scheme and leap-frog time stepping. Land-surface processes are parametrized following Noilhan and Planton (1989). The model was applied using one-way grid nesting with two nested levels for all cases. Data from the European Centre for Medium-range Weather Forecasts (ECMWF) global model with a 0.25° horizontal resolution were used as initial conditions, and for 6-hourly lateral boundary conditions for the domain with a 9 km grid spacing and a size of 1620 km $\times$1620 km. Within this domain, a 3 km grid spacing domain was nested that was centred over

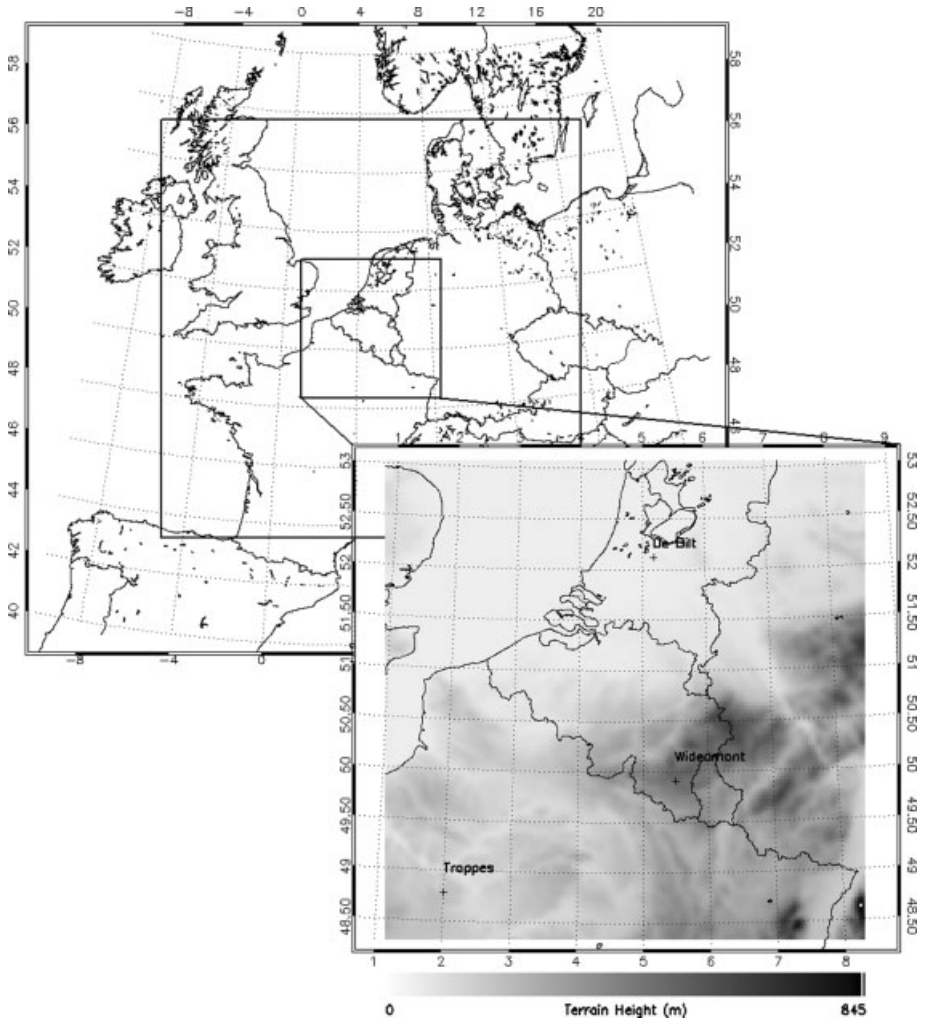

Figure 1. Model domains used for all experiments and all cases. Successive 9 km and 3 km nested domains are denoted by bold rectangles (top left). The inset shows the terrain height of the 3 km domain as well as the location of the radar in Wideumont. Numbers in the margins indicated latitudes and longitudes.

Belgium and covered 540 km ×540 km. Although recent publications mention that a 3 km spatial resolution might be insufficient to fully resolve convective updraughts (e.g. Bryan *et al.*, 2003), this resolution is chosen as being close and relevant to currently used operational NWP model configurations. An overview of the model domains is shown in Figure 1. Fifty vertical levels were used, with a spacing of 20 m near the surface, increasing to 1 km near the upper model boundary located at 20 km. The simulations were initialized with a 6-hour spin-up period that began at 1800 UTC on the previous day. Analyses in the following sections are for the 0000–2400 UTC period, excluding the spin-up period, and for the 3 km domain. Turbulence was represented by the 1.5-order turbulent kinetic energy (TKE) model, and the Sun and Chang (1986) parametrization was used for the convective boundary layer. The Kain and Fritsch (1993) cumulus parametrization was used in the largest domain, while convection was explicitly simulated in the smaller domain. The Lin *et al.* (1983) cloud microphysics parametrization was used, which includes five hydrometeor types (cloud water, cloud ice, rain water, snow and hail). A fourth-order monotonic computational mixing was applied, following Xue (2000), which suppresses numerical noise.

2.2. *Case selection and experiment design*

Two composites containing 15 frontal stratiform cases and 15 convective cases that occurred in Belgium were selected to assess how model modifications affect surface precipitation and cloud properties. Selection of these cases was based on visual inspection of radar-derived precipitation observations during the warm seasons of 2006, 2007 and 2008, so that no frozen surface precipitation was involved. Cases with the largest domain-average 24-hour precipitation accumulations were selected when they exhibited either predominately convective or stratiform signatures. Nevertheless, it cannot be denied that some stratiform (convective) cases do include a limited number of convective (stratiform) areas. In the remainder of this article, stratiform (convective) cases refer to the 15 selected events within the stratiform (convective) composite. An overview of all selected cases is provided in Table 1.

The Lin *et al.* (1983) cloud microphysics scheme used in the control experiment is a one-moment bulk scheme where all precipitating hydrometeors are represented by exponential size distributions of the form:

$$N_x(D) = N_{0x} \exp(-\lambda_x D_x), \quad (1)$$

Table 1. Overview of all cases in the stratiform and the convective composite (day/month/year).

Convective composite	Stratiform composite
05/05/2006	07/05/2006
13/05/2006	17/05/2006
30/05/2006	26/05/2006
25/06/2006	03/08/2006
27/08/2006	14/08/2006
31/05/2007	24/09/2006
11/06/2007	22/10/2006
20/07/2007	07/05/2007
03/09/2007	09/05/2007
01/05/2008	17/05/2007
29/05/2008	28/05/2007
02/06/2008	23/07/2007
22/06/2008	09/10/2007
03/08/2008	29/10/2007
08/08/2008	05/10/2008

where N_x is the number of particles per unit volume per unit size range (m^{-3} m^{-1}), D is the maximum dimension of a particle (m), and N_{0x} (m^{-4}) and λ_x (m^{-1}) are the intercept and slope of the exponential size distribution, respectively. The subscript x denotes the water species (rain, snow or hail). While the intercept parameters are assumed constant, the slope parameters assume all hydrometeors to be constant-density spheres and are determined by:

$$\lambda_x = \left(\frac{\pi \rho_x N_{0x}}{\rho q_x}\right)^{0.25}, \tag{2}$$

where ρ_x is the hydrometeor density ($kg\,m^{-3}$), q_x is the hydrometeor mixing ratio ($kg\,kg^{-1}$), and ρ is the air density ($kg\,m^{-3}$). In the baseline simulation, the precipitating rimed ice species has size distribution properties typical of hail, as described in Lin *et al.* (1983). An overview of the relations used in the baseline simulation (further referred to as ExpH) is listed in Table 2.

A first experiment was applied to all 30 cases to understand, for a broad range of atmospheric conditions, the impact that assumptions about the prescribed size distributions for the precipitating rimed ice species have on clouds and surface precipitation (further referred to as ExpG). To compare with earlier studies, we followed the approach of Gilmore *et al.* (2004). We modified the intercept and density assumptions for hail used in ExpH to those typical of soft graupel (Table 2), but kept the terminal fall velocity formulation following Wisner *et al.* (1972). Note that the choice between graupel and hail as the rimed ice species is an issue in one-moment (Gilmore *et al.*, 2004) and multi-moment schemes (Morrison and Milbrandt, 2011). Schemes that include both species (Milbrandt and Yau, 2005) still have considerable uncertainty on how to implement the graupel-to-hail conversion, and simulations strongly depend on which species prevails (Van Weverberg *et al.*, 2012).

A second experiment was designed to understand how more realistic assumptions used for the snow size distribution affect the quantitative precipitation forecast and cloud fields (further referred to as ExpGS). The baseline simulation (ExpH) and ExpG use a constant intercept for the snow size distribution, even though this parameter is known to vary over several orders of magnitude (Houze *et al.*, 1979). Therefore, we calculate the intercept, N_{0S}, applying the Houze *et al.* (1979) temperature-dependent relation:

$$N_{0S} = 0.02 \exp\{0.12(T_0 - T)\}, \tag{3}$$

where T is the air temperature (K) and T_0 is 273.16 K. This relation better represents the aggregation of snowflakes as temperature increases closer to the surface. Further, while

Table 2. Overview of the formulations for the intercept parameter (N_{0x}, cm^{-4}), slope parameter (λ_x, cm^{-1}), terminal fall velocity (V_x, cm s^{-1}) and density (ρ_x, $g\,cm^{-3}$) for all precipitating hydrometeors used in experiments ExpH, ExpG and ExpGS, where the subscript x denotes rain (R), snow (S) or hail (H). C_D in the hail fall speed formulation for ExpH and ExpG is the drag coefficient, with a value of 0.6. A dash indicates identical formulations as in ExpH.

	ExpH	ExpG	ExpGS
N_{0R}	*0.08* (Marshall and Palmer, 1948)	–	–
λ_R	$\left(\frac{\pi \rho_R N_{0R}}{\rho q_R}\right)^{0.25}$	–	–
V_R	$\frac{2115\Gamma(4+0.8)}{6\lambda_R^{0.8}}\left(\frac{\rho_0}{\rho}\right)^{1/2}$ (Liu and Orville, 1969)	–	–
N_{0S}	0.03 (Gunn and Marshall, 1958)	–	$0.02 \exp 0.12(T_0 - T)$ (Houze *et al.*, 1979)
λ_S	$\left(\frac{\pi \rho_S N_S}{\rho q_S}\right)^{0.25}$ (Lin *et al.*, 1983)	–	$\left(\frac{0.0069 N_{0S}\Gamma(2+1)}{\rho q_S}\right)^{1/(2+1)}$ (Cox, 1988)
V_S	$\frac{152.93\Gamma(4+0.25)}{6\lambda_S^{0.25}}\left(\frac{\rho_0}{\rho}\right)^{1/2}$ (Locatelli and Hobbs, 1974)	–	$\frac{148.07\Gamma(0.527+2+1)}{\lambda_S^{0.527}\Gamma(2+1)}\left(\frac{\rho_0}{\rho}\right)^{1/2}$ (Cox, 1988)
N_{0H}	0.0004 (Federer and Waldvogel, 1975)	4.000 (Gilmore *et al.*, 2004)	4.000 (Gilmore *et al.*, 2004)
λ_H	$\left(\frac{\pi \rho_H N_H}{\rho q_H}\right)^{0.25}$ (Lin *et al.*, 1983)	–	$\left(\frac{0.0702 N_{0H}\Gamma(2.7+1)}{\rho q_H}\right)^{1/(2.7+1)}$ (Locatelli and Hobbs, 1974)
V_H	$\frac{\Gamma(4.5)}{6\lambda_H^{0.5}}\left(\frac{4g\rho_H}{3C_D\rho}\right)^{1/2}$ (Wisner *et al.*, 1972)	–	$\frac{351.63\Gamma(0.37+2.7+1)}{\lambda_H^{0.37}\Gamma(2.7+1)}\left(\frac{\rho_0}{\rho}\right)^{1/2}$ (Locatelli and Hobbs, 1974)
ρ_H	0.913	0.400	0.400

assuming constant-density spheres might be reasonable when calculating the slope parameter λ_R for raindrops, this is not the case for snowflakes. Therefore, λ_S was calculated using:

$$\lambda_S = \left(\frac{a_m N_{0S} \Gamma(b_m + 1)}{\rho q_S}\right)^{1/(b_m+1)}, \quad (4)$$

where a_m and b_m are constants for the mass–diameter (m–D) relation $m_x = a_m D_x^{b_m}$ that were empirically derived for dendritic snow by Cox (1988) (parameters listed in Table 2). Snow terminal fall velocity, V_S ($m\,s^{-1}$), was also calculated assuming a bulk distribution of non-spherical particles, giving:

$$V_S = \frac{a_v \Gamma(b_m + b_v + 1)}{\lambda_S^{b_v} \Gamma(b_m + 1)}, \quad (5)$$

where the empirical constants a_v and b_v were obtained from Cox (1988; see Table 2). Similarly, graupel was no longer represented as constant-density spheres and Eqs (4) and (5) were applied, respectively, to the calculations of slope λ_G and fall velocity V_G. Constants a_m, b_m, a_v and b_v were obtained from the lump graupel observations of Locatelli and Hobbs (1974; see Table 2). It should be mentioned that, while the modified representation of the snow size distribution might be a more realistic approach compared to the original assumptions for constant-density spheres in Lin *et al.* (1983), it does not fully account for the variation of vapour diffusion with the shape of snow and graupel. Woods *et al.* (2007) for instance showed a pronounced impact on the three-dimensional precipitation structure applying such a habit-prediction for a cold frontal rain band, in which the empirical constants a_m and b_m were varied in accordance with particle vapour diffusion differences for temperature and moisture regimes.

An overview of the size distribution assumptions applied in all experiments is given in Table 2. Note that in two-moment bulk microphysics schemes, where number concentration is explicitly predicted, the constant intercept parameter is no longer an issue. The representation of precipitating ice as constant-density spheres still is used in many two-moment schemes; hence, results presented here might be relevant to those schemes as well. It is stressed that we are mainly focussing on the operational model set-ups, in which one-moment schemes are still the workhorse at this time.

2.3. Observational data

2.3.1. Satellite data

To evaluate the cloud phase, we applied the approach of the International Satellite Cloud Climatology Project (ISCCP) to sort clouds into nine classes according to their cloud-top pressure (CTP) and cloud optical thickness (COT) (Rossow and Schiffer, 2001). These classes include cirrus, cirrostratus, deep convection, altocumulus, altostratus, nimbostratus, cumulus, stratocumulus and stratus. Thresholds in cloud-top pressure were used to separate low and middle cloud (680 hPa) and middle and high cloud (410 hPa), which were applied to the satellite-retrieved and simulated clouds. The CTP threshold between middle and high cloud is modified slightly from that in Rossow and Schiffer (2001), since all cases simulated here were associated with warm-season deep precipitating clouds and their criterion was generalized for global use for all seasons.

Satellite data were used from the Spinning Enhanced Visible and Infrared Imager (SEVIRI) on-board the geostationary Meteosat-8 satellite by the EUMETSAT Satellite Application Facility on Climate Monitoring (CM-SAF: Schulz *et al.*, 2009). Observed COT and CTP were derived from these data using algorithms described in Roebeling *et al.* (2006). The SEVIRI instrument senses the atmosphere in four visible and near-infrared channels, and eight infrared channels. COT and CTP data are available at 3 km ×6 km horizontal resolution in the study area with an image repeat cycle of 60 minutes. Since the visual channel is required for COT retrievals, only daytime hours are included in the analysis. Data were missing for two stratiform cases (26 May 2006 and 24 September 2006). Uncertainties associated with CM-SAF retrieved COT are well described, for example, by Bugliaro *et al.* (2010). A correlation coefficient of 0.79 and a mean standard deviation of 0.92 were obtained between CM-SAF and their ground-truth COTs. Liquid-water clouds showed the best agreement, while a slight overestimation was present in ice clouds with COT > 2 and mixed-phase clouds. COT in ARPS is calculated for each hydrometeor separately, following a routine developed at the National Aeronautics and Space Administration (NASA) Goddard Cumulus Ensemble Modelling Group (Tao *et al.*, 2003). For liquid-water clouds and hail, COT in the visible region is parametrized based on Sui *et al.* (1998) assuming spherical droplets:

$$\tau_c = 1.5 \times \int \frac{q_c}{R_{ec}} dz, \quad (6)$$

$$\tau_r = 1.5 \times \int \frac{q_r}{R_{er}} dz, \quad (7)$$

$$\tau_h = \int \frac{q_h}{R_{eh}} dz, \quad (8)$$

where q_c, q_r and q_h are the mixing ratios (in $kg\,kg^{-1}$) of cloud water, rain and hail, respectively. Their effective radii (in cm) are given by $R_{ec} = 0.0015, R_{er} = \frac{3.0}{(\pi N_{0r}\rho_r/\rho q_r)^{0.25}}$, and $R_{eh} = \frac{3.0}{(\pi N_{0h}\rho_h/\rho q_h)^{0.25}}$. For cloud ice and snow, COT is parametrized based on a formula derived for cirrus ice crystals by Fu and Liou (1993):

$$\tau_{is} = \int 10^4 \times (q_i + q_s) \times \left(0.006656 + \frac{3.686 \times 10^{-4}}{R_{eis}}\right) dz, \quad (9)$$

where q_i and q_s are the mixing ratios ($kg\,kg^{-1}$) of cloud ice and snow, respectively. The effective radii (in cm) are temperature-dependent: $R_{eis} = 0.0125$ if temperature (T) is above 243.16 K, $R_{eis} = 0.0025$ if temperature is below 223.16 K, and $R_{eis} = 0.0125 + (T - 243.16) * 0.0005$ if temperature is between 223.16 and 243.16 K. The empirical coefficients are obtained from Fu and Liou (1993) by fitting scattering calculations to observed snow size distribution data. Total COT is the sum of all components described in Eqs (6) to (9). As the satellite cannot discriminate between values above 100, all simulated values higher than this value were thresholded to 100.

ARPS-simulated CTP is defined as the pressure at the effective emission height of the cloud, which is computed as the level where the integrated long-wave absorption COT (from the model top downwards) reaches a value of one (Luo *et al.*, 2010). For consistency with this value, short-wave COT > 2 has been considered in the satellite and model analyses (since short-wave extinction COT is about double the mid-infrared absorption COT). The value of this threshold is somewhat arbitrary, but the same value is applied to the satellite and model fields. A lower value would detect more cloud occurrence in both fields, but retrieved COT at lower values becomes more uncertain because of increased complications presented by the variable land-surface albedo and the increased chance of interpreting multi-layered clouds (i.e. thin cirrus overlying low-level cloud). A sensitivity study using a short-wave COT threshold of one changes the cloud occurrences but not the overall quality of the model–satellite agreement. In this article, the observed and simulated COT and CTP data were both sampled at hourly intervals.

2.3.2. *Surface precipitation data*

Surface precipitation observations are obtained from the C-band weather radar in Wideumont (Figure 1), operated by the Royal Meteorological Institute of Belgium, and from a dense network of rain-gauges (1 per 135 km^2), operated by the hydrological service of the Walloon region. Ground clutter was removed using a time-domain Doppler filter as well as by an additional treatment, based on a static clutter map. Radar-based precipitation estimates are derived from a pseudo-CAPPI (Constant Altitude Plan Position Indicator) at 1500 m above sea level, extracted from a five-elevation scan. The processing of the radar data and strategies for merging radar observations with rain-gauge measurements are presented in Goudenhoofdt and Delobbe (2009). The 24 h precipitation accumulations for convective and stratiform events were calculated using a simple mean-field bias adjustment and were aggregated to the ARPS grid. The underlying assumption of this method is that radar estimates are affected mainly by a uniform multiplicative error, due to bad electronic calibration or an erroneous coefficient in the reflectivity–rain-rate relation. A four-year verification of this method against an independent set of rain-gauge stations found the absolute error of this technique to be about 1.8 mm (Goudenhoofdt and Delobbe, 2009). This uncertainty is associated with many issues regarding the quality of the returned power radar signal, such as beam blocking by intense convective cells or beam broadening and attenuation at large distances from the radar. To partly account for these uncertainties, data farther than 150 km from the radar were omitted from analyses of the observed and simulated fields.

3. Results

3.1. *Cloud optical thickness*

3.1.1. *Stratiform composite*

Figure 2(a) shows the frequency distributions of satellite-retrieved and simulated cloud optical thickness for the 15 cases in the stratiform composite. COT thresholds discriminating thin, intermediate and thick clouds, according to Rossow and Schiffer (2001), are denoted by dotted vertical lines. Unlike many previous studies (e.g. Karlsson *et al.*, 2008; Otkin and Greenwald, 2008), the fraction of optically thick clouds in the baseline simulation (ExpH) is quite well simulated compared to SEVIRI. On the other hand, the frequency of thin clouds is overestimated. Figure 3 and Table 3 show that the domain-averaged COT is slightly underestimated for most cases in ExpH, mainly due to the underestimated cloudiness (and hence a larger fraction of clear sky; Table 4). To assess how the overestimation of COT affects the transmission of radiation through the atmospheric column, a transmission-weighted average COT

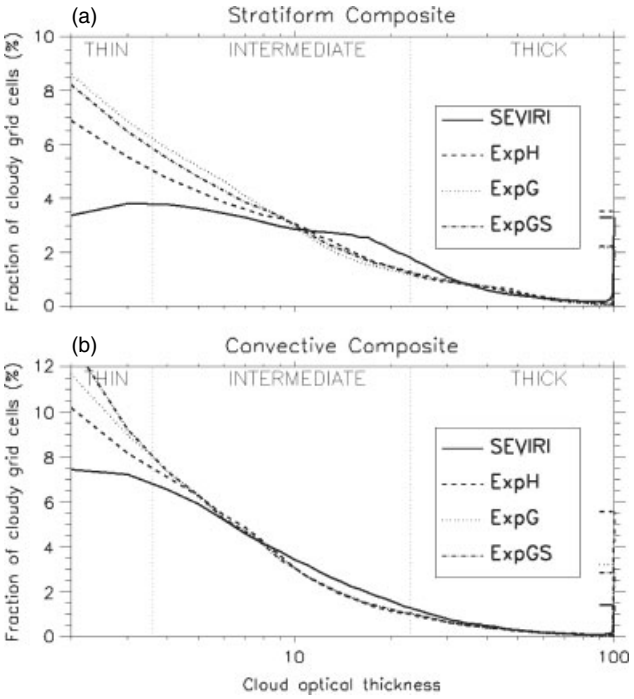

Figure 2. Frequency distribution of cloud optical thickness for all experiments in (a) the stratiform composite, and (b) the convective composite. Only daytime hours and clouds with COT > 2 are used. Vertical dotted lines denote the threshold between thin and intermediate and intermediate and thick clouds according to Rossow and Schiffer (2001). The horizontal lines at the COT level of 100 denote the fraction of cloudy grid cells with COT larger than 100 for SEVIRI and each of the experiments.

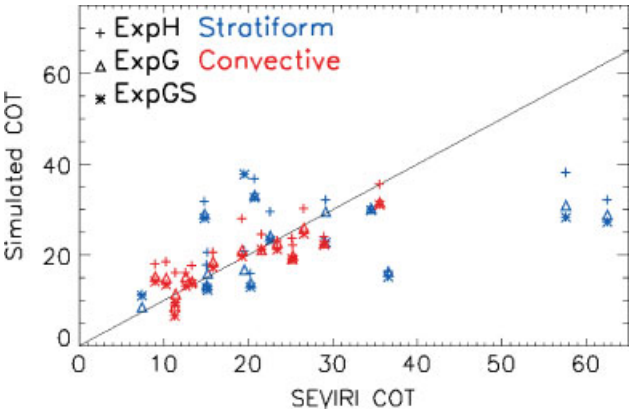

Figure 3. Observed vs. simulated domain- and time-averaged cloud optical thickness for all cases and all experiments. Stratiform cases are in blue and convective cases are in red. The different experiments are denoted with different symbols as indicated in the top panel. The 1:1 line is provided as reference (symbols above this line indicate model overestimation, symbols below this line model underestimation).

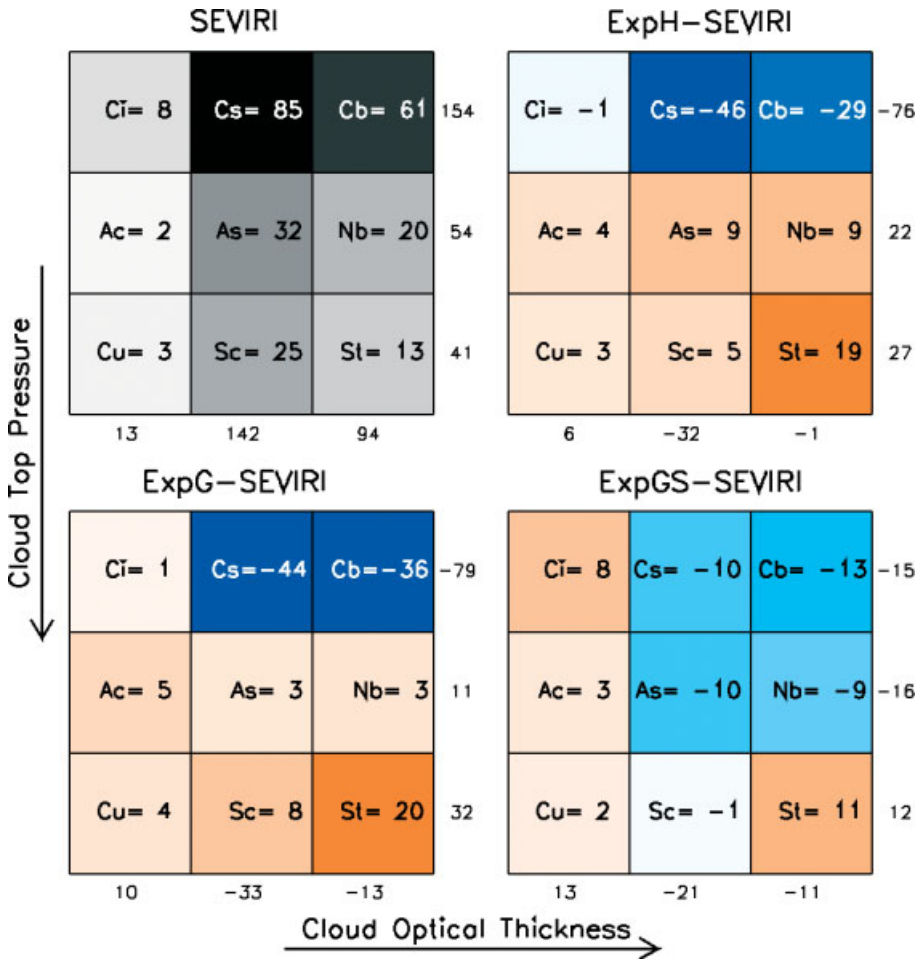

Figure 4. Cloud classification according to ISCCP, based on COT and CTP for all experiments in the stratiform composite. The top left panel (SEVIRI) shows the time- and case-averaged area covered by each cloud class as observed by SEVIRI (in 1000 km^2). Shading is applied according to the numbers (from white for low values to black for high values). The remaining panels show the difference in time- and case-averaged area between the respective experiments and SEVIRI, where colour shading ranges from blue, for model underestimation, to red for model overestimation. Abbreviations of cloud classes: cirrus (Ci), cirrostratus (Cs), cumulonimbus (Cb), altocumulus (Ac), altostratus (As), nimbostratus (Nb), cumulus (Cu), stratocumulus (Sc) and stratus (St). Thresholds in cloud-top pressure are 410 hPa between high and middle clouds, and 680 hPa between middle and low clouds. Thresholds in cloud optical thickness are 3.6 between thin and intermediate clouds, and 23.0 between intermediate and thick clouds. Numbers to the right and below each figure denote, respectively, the row and column totals.

is computed over the domain and over the available output times, $\bar{\tau}$, following Schröder *et al.* (2006):

$$\bar{\tau} = -\mu \ln\left(1/(1N)\sum_i \exp(-\tau_i/\mu_i)\right), \qquad (10)$$

where μ is the arithmetically averaged solar zenith angle over the domain, N is the number of grid cells times the number of output times, and μ_i and τ_i are, respectively, the cosine of the solar zenith angle and the optical thickness of grid cell i. Hence optical thickness is first transformed to direct-beam transmission (i.e. Beer's Law), before calculating the spatial average and then transformed back to optical thickness. Table 3 shows that, due to the overestimation of the thin cloud fraction and the underestimated cloudiness, the transmission-averaged COT (calculated following Eq. (11)) is significantly underestimated. Indeed, from a transmission point of view, the overestimation of the frequency of very thin clouds (COT <3; Figure 2(a)) is much more important than the overestimation of the frequency of thick clouds.

Replacing the hail size distribution formulations for the rimed ice species with those typical of small graupel (ExpG), the fraction of very thick clouds is underestimated and the overestimation of optically thin clouds in ExpH further deteriorates. This leads to an underestimation in both the domain average (Figure 3) and the transmission-averaged COT (Table 3). Despite a still significant overestimation of the thin cloud fraction (of *cloudy grid* cells only; Figure 2(a)), ExpGS has a somewhat better *domain-average* COT compared to ExpG, due to the better captured total cloudiness (Table 4). Transmission-averaged COT is even closer to the observations compared to ExpH, although an important underestimation remains and too much shortwave radiation would reach the surface on average.

When information of COT is combined with information on the CTP, a classification of clouds according to the ISCCP approach can be obtained (Rossow and Schiffer, 2001). Figure 4 shows the time- and case-averaged surface area covered by each of the nine ISCCP classes for the stratiform composite as derived from SEVIRI, and for the differences in surface area of each of the classes between the experiments and SEVIRI. From the COT distribution on this figure, it is clear that the underestimated cloudiness in ExpH mainly stems from a lack of intermediate clouds. More importantly, the clouds tend to be positioned too low in the atmosphere as the surface area covered by high

Table 3. Overview of statistics on observed and simulated COT in the stratiform and the convective composite for all experiments and averaged for all cases.

Case	Satellite	ExpH	ExpG	ExpGS
Average Stratiform	25.4 (2.1)	19.2 (1.2)	16.3 (1.1)	18.2 (1.4)
Bias Stratiform	–	−6.2(−0.9)	−9.1(−0.9)	−7.2(−0.7)
RMSE Stratiform	–	14.4 (1.4)	16.0 (1.4)	16.0 (1.2)
Average Convective	16.0 (1.4)	11.0 (0.6)	9.2 (0.6)	9.6 (0.7)
Bias Convective	–	−5.1(−0.7)	−6.8(−0.8)	−6.4(−0.7)
RMSE Convective	–	6.8 (0.9)	8.3 (0.9)	7.8 (0.8)

Domain- and time-averaged COT (transmission-averaged between parentheses); Bias of the domain- and time-averaged COT; Root-Mean-Squared Error of the domain and time averaged COT. None of the simulated average values were significantly different from the observations, based on a Wilcoxon Rank-Sum test (at the 10% confidence level). Averaging has been performed over daytime hours only for a fair comparison against the observations.

Table 4. Mean cloudiness for all experiments during the stratiform events and convective events, averaged over all cases.

	Stratiform Mean cloudiness (%)	Convective Mean cloudiness (%)
Satellite	90.0	78.7
ExpH	71.9	47.5
ExpG	68.8	45.3
ExpGS	77.6	49.8

Cloudy grid cells are defined as grid cells with COT >2. Averaging is done over the entire 3 km domain for daytime hours only.

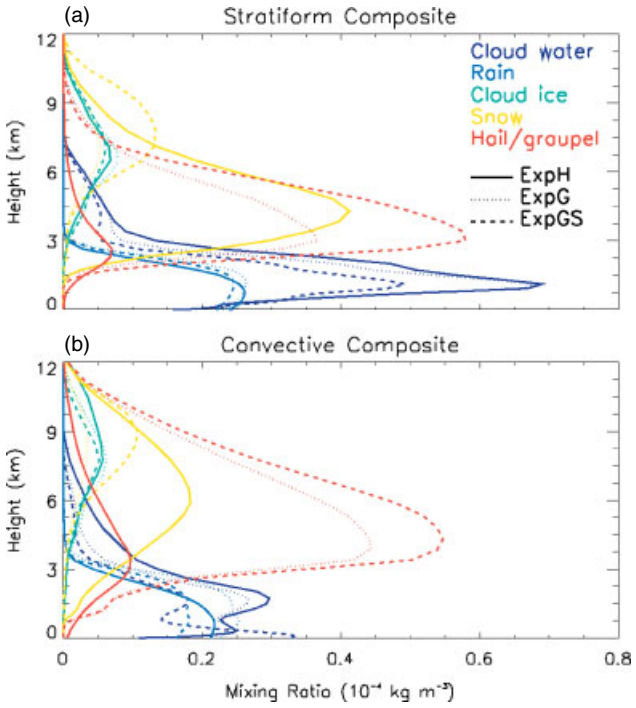

Figure 5. Domain-average vertical profiles of snow (yellow), graupel (red), cloud water (dark blue), rain water (blue) and cloud ice (green) mixing ratio for each of the experiments in the (a) stratiform composite and (b) convective composite. Averaging is for the entire domain and over all cases and output times.

clouds in ExpH is only half as large as in the observations. While the areal extent of clouds categorized as cirrostratus and cumulonimbus clouds is largely underestimated, the extent of nimbostratus, altostratus and stratocumulus clouds is somewhat overestimated. This is consistent with, for example, Keil *et al.* (2003) who found a lack of high clouds for two winter storm simulations in Europe using a one-moment bulk microphysics scheme. Karlsson *et al.* (2008), however, found more high-level clouds in their simulations, although they had a rather low boundary (500 hPa) between high and mid-level clouds.

Although these results apply to the stratiform composite, we find a rather large number of clouds categorized as cumulonimbus in the simulations and observations. This might be because the classification method cannot discriminate multilayer clouds. Hence, when thin cirrus or cirrostratus clouds overlie a thick stratus cloud, it will be classified as cumulonimbus. The naming convention in Figure 4 follows that of the ISCCP approach. Given the aforementioned limitations, cumulonimbus and nimbostratus classified clouds might not all be precipitating, as they might well be associated with thin cirrus overlying a thick non-precipitating stratus cloud. However, since cloud-top height in the model was determined based on infrared COT similar to how satellite discriminates cloud tops, the model and observations would be affected equally by this limitation. Therefore this limitation is not expected to influence the model–observation comparison, but it should be understood that this method will likely overestimate the occurrence of thick, high cumulonimbus clouds.

Replacing the large hail by graupel (ExpG) does not significantly affect the COT distribution (as shown by the column totals in Figure 4), while the cloud tops are still too low as well. The ExpG still leaves the cirrostratus and cumulonimbus clouds largely underestimated. A better representation of the snow size distribution (ExpGS) slightly improves the areal extent of intermediately thick clouds and slightly deteriorates the occurrence of thick clouds (Figure 4). On the other hand, this experiment dramatically improves the position of cloud tops. The area occupied by cirrostratus clouds and cumulonimbus clouds (which might well be high thin clouds overlying low thick clouds, as outlined before) is brought into much closer correspondence with observations by this experiment.

To gain insight into the reasons for differences between the experiments, Figure 5(a) shows the domain-average vertical profiles of the hydrometeors for the stratiform composite. The main difference between ExpH and ExpG is the prevalence of snow and graupel below 7000 m altitude. ExpH is clearly snow-dominated, while ExpG is graupel-dominated. According to Eq. (9), the radiation scheme considers snowflakes to be large at lower altitudes and almost optically invisible. Graupel is treated as being large, regardless of the altitude at which it resides. Therefore, despite important differences in the vertical profiles of graupel and snow, no clear change of the COT distributions

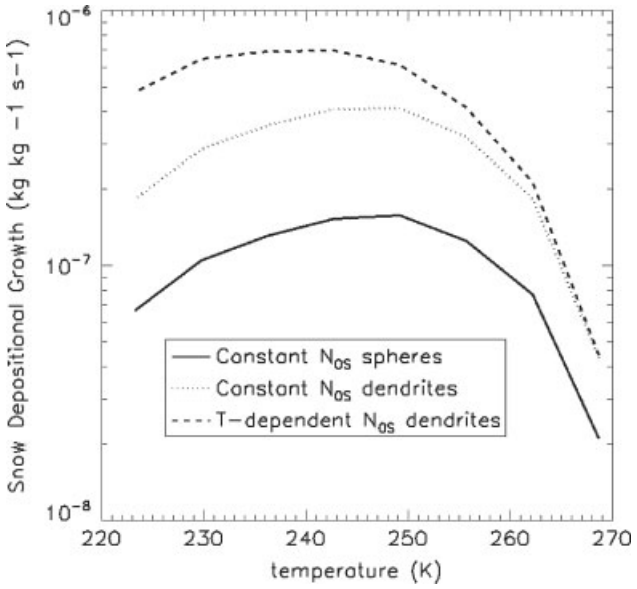

Figure 6. Theoretical snow depositional growth rates as a function of temperature for spherical particles and constant intercept (as in the original Lin *et al.* (1983) scheme), for dendritic particles and constant intercept (following Cox, 1988), and for dendritic particles and temperature-dependent intercept (following Cox, 1988; Houze *et al.*, 1979). Snow mixing ratio was varied between 0.05 and 0.5 $g\,kg^{-1}$, as in a deep precipitating snow cloud, after Thompson *et al.* (2004).

occurs between the ExpH and ExpG. The improved representation of the snow size distribution (ExpGS) clearly shifts the snow maximum to higher altitudes (Figure 5(a)). Since snow mixing ratios at high altitudes are associated with smaller-sized crystals according to Eq. (9), the shift of the snow content maximum to higher altitudes in ExpGS significantly impacts the vertical extent of clouds. The two modifications made to the snow size distribution in this experiment involved a temperature-dependent intercept parameter (N_{0S}) and the introduction of non-spherical particles. Both of these modifications have been shown before to enhance the depositional growth of snow at high altitudes in case-studies. Thompson *et al.* (2004) have shown this for the temperature-dependent N_{0S} in an idealized simulation of orographic precipitation, and Woods *et al.* (2007) found this for non-spherical snow particles in a real-case simulation of a cold-frontal rain band. Figure 6 shows the impact of these modifications to the snow size distribution on the theoretical snow depositional growth as a function of temperature. It is clear that the modified m–D relation, following Cox (1988), (as opposed to the constant-density sphere assumption in ExpG and ExpH) and the temperature-dependent N_{0S} (as opposed to the constant N_{0S} in ExpG and ExpH) increases the depositional growth mainly at low temperatures. At lower altitudes (and hence warmer temperatures), snow content in ExpGS rapidly decreases as snow particle size grows and graupel collects most of it (Figure 5(a)). Note that a temperature-dependent mixing ratio is able to represent the aggregation of snowflakes from small particles at low temperatures to large particles at high temperatures. To some extent, this mimics the behaviour in a two-moment microphysics scheme. For example, Milbrandt *et al.* (2010) showed that snow depositional growth increases in two-moment schemes compared to a one-moment scheme with a constant N_{0S}, although this was associated with excessive snow contents. Given the computational efficiency of one-moment schemes, it should be further investigated to what extent one-moment schemes with diagnostic N_{0S} can mimic features associated with two-moment schemes, such as aggregation and size sorting. A more detailed analysis of the impact of the different experiments on cloud properties will be provided for a selected case-study in section 3.3.1.

3.1.2. *Convective composite*

For the set of 15 convective cases, Figure 2(b) shows a somewhat different behaviour of the ExpH than for the stratiform composite. Compared to observations, too large a fraction of total cloudy area consists of very optically thick clouds (COT >100) or thin clouds (COT >3) in the simulations. However, due to a strong underestimation of the cloudiness (Table 4), the domain-averaged COT (including the clear-sky area) and the transmission-averaged COT show an important underestimation bias (as indicated by the negative bias in Table 3), indicating that too much short-wave radiation would reach the surface in most convective cases. The frequency of optically very thick clouds is slightly better captured when large hail is replaced by small graupel (ExpG; Figure 2(b)). However, the overestimation in the frequency of thin clouds becomes worse. Moreover, cloudiness is further reduced and hence the underestimation of domain-averaged COT further deteriorates. Further modifying the representation of the snow (and graupel) size distribution (ExpGS) further deteriorates the overestimation of thin clouds but, as mean cloudiness becomes slightly larger, domain-averaged and transmission-averaged COT slightly improve.

Figure 7 provides the areal extent for each cloud class according to the ISCCP classification for the observations and each experiment. This figure clearly shows the general underestimation of cloudiness, indicated by the prevailing blue colours. This figure also shows that, similar to the stratiform composite, an improvement in the representation of clouds becomes apparent in ExpGS compared to ExpG and ExpH. More cirrostratus is present at the expense of low and middle clouds, bringing the fraction of high clouds into closer correspondence with the observations, although there remains an important underestimation.

It might seem odd that the area covered by cumulonimbus clouds in the convective composite is rather small. However, note that all daytime hours are used regardless of when deep convective clouds are present; so the composite will also include the shallow and thin clouds that frequently precede or occur between the convective towers.

The reasons for the improvement in the CTP distributions can be assessed from Figure 5(b). Compared to the stratiform composite, a similar sensitivity of the snow and graupel content to the representation of the largest precipitating ice species (ExpH vs. ExpG) is found in the convective composite. Again, due to the large sizes of these species, this does not lead to clear differences in the COT distributions. ExpGS resembles ExpG apart from the fact that the snow maximum is lofted to higher altitudes, as explained in the previous section for the stratiform composite. In terms of the metrics presented here, increased snow depositional growth at high altitudes, associated with the applied size distribution modifications, improves model–observation agreement for stratiform and convective conditions. This supports that similar findings for single case-studies of stratiform

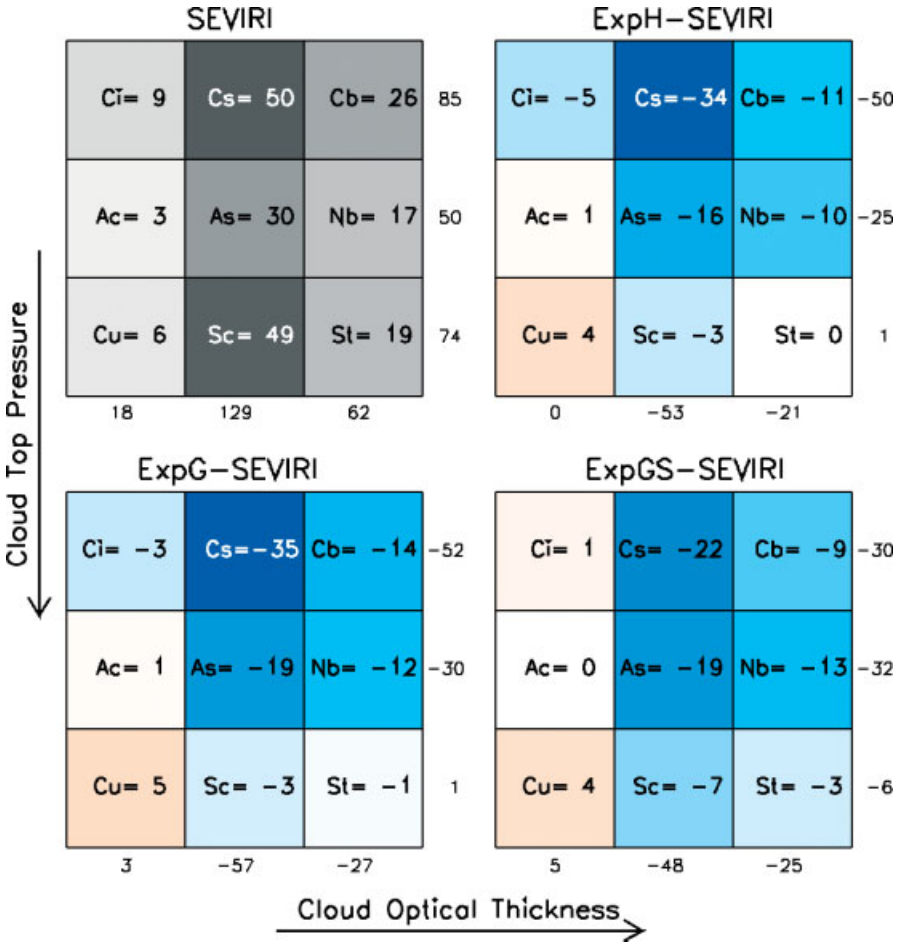

Figure 7. As in Figure 4, but for the convective composite.

precipitation (e.g. Thompson *et al.*, 2004; Colle *et al.*, 2005; Woods *et al.*, 2007) can be generalized to a broad range of synoptic conditions and can cautiously be interpreted as model improvements.

3.2. *Surface precipitation*

3.2.1. *Stratiform composite*

Table 5 and Figure 8(a) and (b) provide an overview of the domain average and maximum 24-hour (0000–2400 UTC) accumulated surface precipitation for all experiments, and as derived from combined radar and rain-gauge information for the stratiform composite (blue symbols). Domain-average surface precipitation in ExpH shows an overestimation of about 25% (Table 5), and domain-maximum accumulations are even overestimated by over 50%. Considerable variation exists for different cases, with some cases overestimating surface precipitation by more than 100% while others underestimate it (Figure 8(a) and (b)). In contrast to many previous studies, which found a strong reduction in surface precipitation by replacing large hail by small graupel, no such impact was found in our stratiform composite (ExpG; Table 5). Viewing the composite averages, no significant reductions in domain-average or maximum precipitation are found as compared to ExpH. For individual cases, the differences generally remain within 10% of ExpH. A 20% increase in domain-average surface precipitation occurs in ExpGS (Table 5 and Figure 8), compared to ExpG. All but one case in the stratiform composite have higher domain-average surface precipitation accumulations in ExpGS as compared to the other experiments, while the domain-maximum precipitation decreases slightly in most cases (Figure 8).

Although ExpG and ExpH behave similarly in terms of surface precipitation, there are notable differences in the vertical distribution of hydrometeors (Figure 5(a)). As mentioned in the previous section, snow above the melting layer is prevalent in ExpH, while graupel is prevalent in ExpG. Summing the hail/graupel and snow downward mass fluxes yields similar fluxes near the melting layer between ExpH and ExpG (not shown). Fluxes of graupel near the melting layer are somewhat higher in ExpGS, which also enhances rain mass flux since this mainly originates from melting graupel. A more detailed analysis of the reasons for differences in surface precipitation accumulation between ExpGS and the other experiments is outlined in section 3.3.1.

3.2.2. *Convective composite*

The simulations in the convective composite tend to produce excessive surface precipitation. From Figure 8(a) and (b) (red symbols) and Table 5, virtually all convective simulations considerably overestimate the domain-average and maximum surface precipitation in ExpH, which results in an all-case overestimation of about 80% (Table 5).

Table 5. Overview of statistics on observed and simulated surface precipitation in the stratiform and the convective composite for all experiments and averaged for all cases.

Case	Radar	ExpH	ExpG	ExpGS
Mean Stratiform	6.6 (39.1)	8.4 (60.7*)	8.1 (65.8*)	9.7* (56.1*)
Bias Stratiform	–	1.8 (22.2)	1.4 (27.2)	2.5 (19.3)
RMSE Stratiform	–	3.6 (39.2)	3.6 (48.4)	4.3 (32.0)
Mean Convective	5.2 (55.9)	9.4* (101.1*)	9.5* (80.9*)	9.1* (70.8)
Bias Convective	–	4.2 (44.9)	4.3 (24.8)	3.9 (14.7)
RMSE Convective	–	5.9 (64.0)	5.8 (35.9)	5.3 (23.5)

Mean, bias and root-mean-squared error (RMSE) of the domain-average 24-hour surface precipitation accumulation. Respective values for the domain-maximum 24-hour surface precipitation accumulation are provided between parentheses. Simulated values significantly different from the observed surface precipitation, based on a Wilcoxon Rank-Sum test (at the 10% confidence level), are denoted with an asterisk.

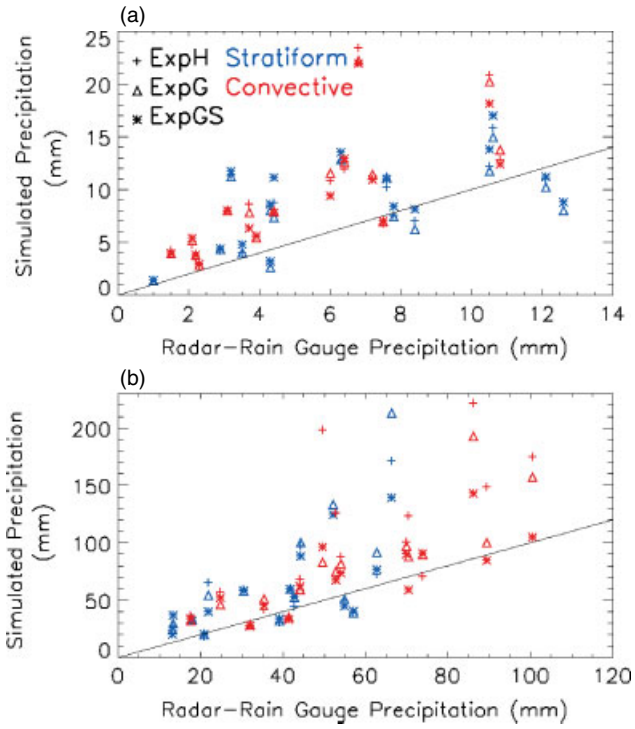

Figure 8. Observed vs. simulated (a) domain-average 24-hour surface precipitation and (b) domain-maximum 24-hour surface precipitation for all cases and all experiments. Stratiform cases are in blue and convective cases are in red. The different experiments are denoted with different symbols as outlined in the top panel. The 1:1 line is provided as reference (symbols above this line indicate model overestimation, symbols below this line model underestimation).

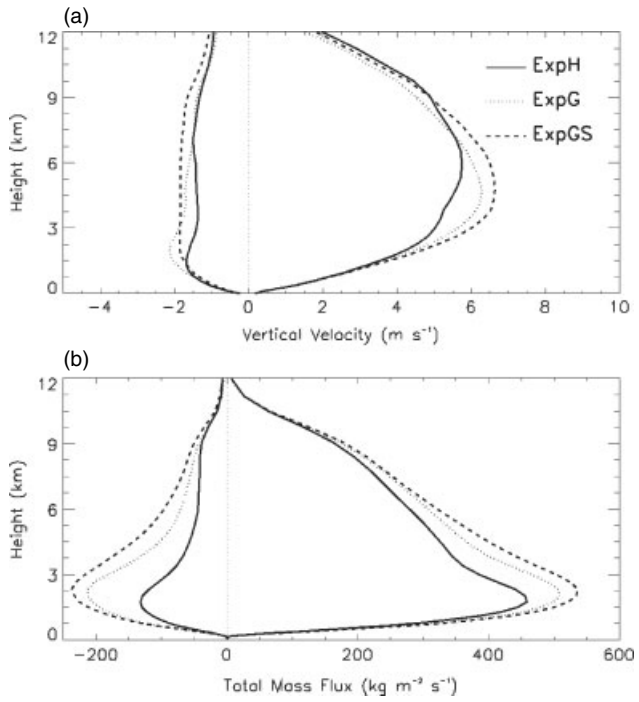

Figure 9. (a) Vertical profiles of domain maximum and minimum vertical velocity for all experiments, averaged over all convective cases, and (b) vertical profiles of updraught and downdraught total mass flux of dry air for all experiments, averaged over all output times and all convective cases.

The results of ExpG suggest a limited impact on domain-average surface precipitation for a large number of real-case simulations (Table 5 and Figure 8). Domain-average surface precipitation for individual cases only varies within about 10% between ExpG and ExpH and on the average for all cases does not show any impact. Note that the convective composite contains a large range of storm types and even during a supercell case (on 22 June 2008) precipitation was only slightly reduced. A more important sensitivity is seen in the domain-maximum precipitation. The average overestimation for all cases in ExpG is reduced to 45% from 80% for ExpH. Further, modifying the snow size distribution assumptions (ExpGS) again hardly impacts the domain-average surface precipitation (Figure 8 and Table 5), but the domain-maximum precipitation overestimation is further reduced to 27%.

In contrast, numerous idealized case-studies of deep convection suggest that replacing large hail by small graupel tends to reduce surface precipitation significantly (Gilmore *et al.*, 2004; van den Heever and Cotton, 2004; Morrison and Milbrandt, 2011). Those idealized studies typically do not include boundary layer and radiation processes and, for supercell simulations, also do not capture the full life cycle of the convection. Hence it is uncertain how this behaviour extrapolates to real-case simulations of deep convection.

By and large, the nature of the largest rimed ice species (graupel or hail) can alter surface precipitation in two possible ways. First, there might be a change in latent heating (e.g. due to more freezing) and hence to the general dynamics of the storm systems. Second, there might be a change in precipitation efficiency of the storm systems, which would lead to differences in surface precipitation since the same amount of total excess water vapour is turned to condensate. For instance, this could be due to changes in sublimation or evaporation of condensed

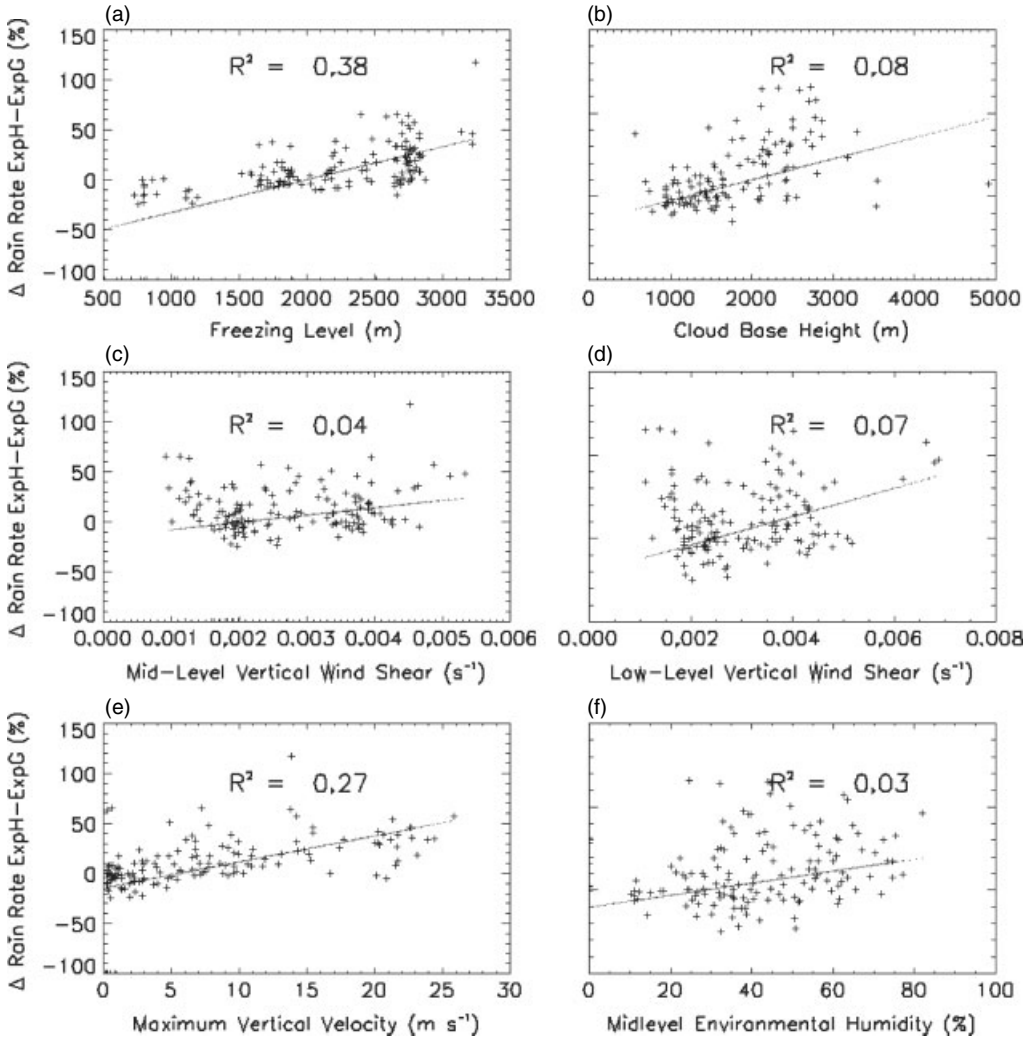

Figure 10. Correlation analysis of the percentage difference in precipitation rate between ExpH and ExpG and different environmental variables. Each data point in the figure denotes this percentage difference in domain-average instantaneous precipitation rate for a particular output time and case (for grid cells exceeding 10 mm h^{-1} only). Factors examined are (a) freezing-level height, (b) cloud-base height, (c) mid-level vertical wind shear (0–6 km), (d) low-level vertical wind shear (0–3 km), (e) maximum vertical velocity and (f) mid-level relative humidity. Coefficients of determination are shown on the respective figures. Lines indicate a linear regression fit through the points.

particles caused by changes in fall speed. Figure 9 provides vertical profiles of the maximum up- and downdraughts, and of the total up- and downdraught mass flux averaged for all convective cases (up/downdraughts are defined as regions ascending/descending at 0.5 m s^{-1}). Updraught mass flux and vertical velocity is larger in the experiments including graupel, which is likely due to enhanced latent heating associated with freezing processes. Indeed, total cloud water is significantly reduced in ExpG compared to ExpH (Figure 5(b)) as more of it is consumed for riming on the more numerous graupel particles (not shown). However, Figure 9 also shows enhanced downdraught mass fluxes and maximum velocities for ExpG, associated with enhanced evaporation and sublimation. Hence, it is likely that in ExpG more vapour is turned to condensate due to more vigorous updraughts, but then more of this condensate is returned to vapour that leads to decreased precipitation efficiency as suggested, for example, by Van Weverberg *et al.* (2011b).

A number of factors might explain the difference between the small impact found for our real-case simulations and the large impact of the precipitating ice species found by previous idealized studies on surface precipitation (Gilmore *et al.*, 2004; van den Heever and Cotton, 2004; Morrison and Milbrandt, 2011). One factor might be that there is much more stratiform precipitation between the convective cells than in a real-case simulation and, therefore, the differences between ExpG and ExpH are somewhat smoothed out. However, the smaller differences between ExpG and ExpH in the domain-maximum precipitation (Table 5), which is associated with convective cells, rules out this hypothesis. In order to investigate the role of other environmental conditions, a correlation analysis was performed between the differences in precipitation rates between ExpH and ExpG and the mean-freezing level, cloud-base height, updraught velocity, vertical-wind shear and mid-level humidity (Figure 10). The coefficient of determination, R^2, is given on each plot. Each data point in Figure 10 represents the difference between ExpH and ExpG in instantaneous domain-average precipitation rate (for a certain case and output time and when grid cells have precipitation intensities of more than 10 mm h^{-1} only). Of the investigated factors, the freezing level (Figure 10(a)) and the updraught velocity (Figure 10(e)) account for the largest part of the explained variance in the difference between ExpH and ExpG. The reason might be derived from Figure 11. Hail in ExpH and graupel in ExpG have

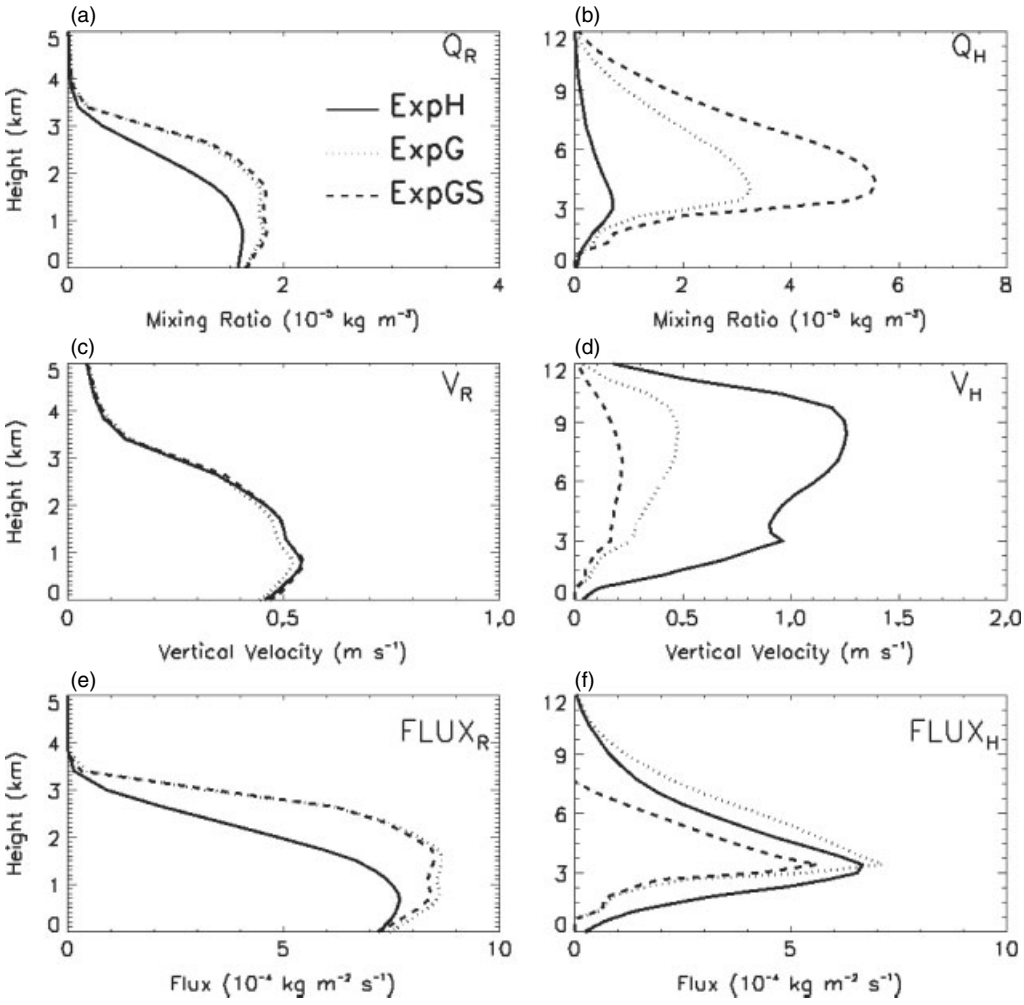

Figure 11. Domain-average vertical profiles of (top) mixing ratio, (middle) fall speed and (bottom) flux for (left) rain and (right) graupel, averaged over all output times and all cases in the convective composite for each experiment.

very different average vertical velocities (Figure 11(c); V_H); however, due to the larger mass content of graupel in ExpG, the averaged downward flux (Figure 11(f); $Flux_H$) of graupel (i.e. larger precipitation rate) around the freezing level is larger as compared to the averaged downward hail flux in ExpH. As most rain originates from melting graupel, averaged downward rain fluxes just below the freezing level are enhanced as well (Figure 11(e); $Flux_R$). However, in ExpH, hail melts very slowly and melting hail continues to add to the rain content down to the surface. In ExpG, graupel melts almost instantaneously at the melting level, leaving more time for rain to evaporate. Hence, due to more rain evaporation in ExpG, the precipitation rates at the surface in ExpH increase to the precipitation rate in ExpG. Thus, the higher the melting level is, the longer that rain will evaporate at a higher rate in ExpG as compared to ExpH, and the more surface precipitation rates deviate between ExpH and ExpG. In that context, it is worth noting that the highest melting level in any of our real cases was situated around 3000 m, while previous idealized experiments were initiated with freezing levels around 4000 m. Further, the stronger the updraughts, the higher that graupel will be lofted, and the more time there is for it to sublimate instead of melting to rain (as suggested by Van Weverberg *et al.*, 2011b). Again, while maximum updraught velocities in our simulations reach about 30 m s^{-1}, updraughts in Gilmore *et al.* (2004) were up to 60 m s^{-1}. Hence, it is likely that the large reduction in surface precipitation found in idealized experiments containing graupel is only valid for certain environmental conditions, which are typical for supercell convection in Midwest USA but not for western Europe. An additional factor that might contribute to different behaviour between the idealized experiments and our real-case simulations is that the idealized simulations were typically rather short (about 2 hours) and might not have captured the full convective cycle.

ExpGS behaves similarly to ExpG, except that the graupel fall speed is even lower (due to the Locatelli and Hobbs (1974) relation used in the fall speed formulation). However, the total graupel mass is also increased and hence the total downward mass flux is similar to that in ExpG. Thus, in contrast to the stratiform precipitation events, ExpGS does not enhance domain-average precipitation during convective cases. Indeed, snow plays a lesser role in the convective composite compared to the stratiform composite (Figure 5(a) and (b)) and hence the enhancement in snow depositional growth in ExpGS might not be sufficient to significantly impact precipitation efficiency.

The general overestimation in all experiments of surface precipitation associated with the convective composite might, to some extent, be related to the coarse resolution of the experiments presented here. Indeed, Deng and Stauffer (2006) suggested that updraughts might become

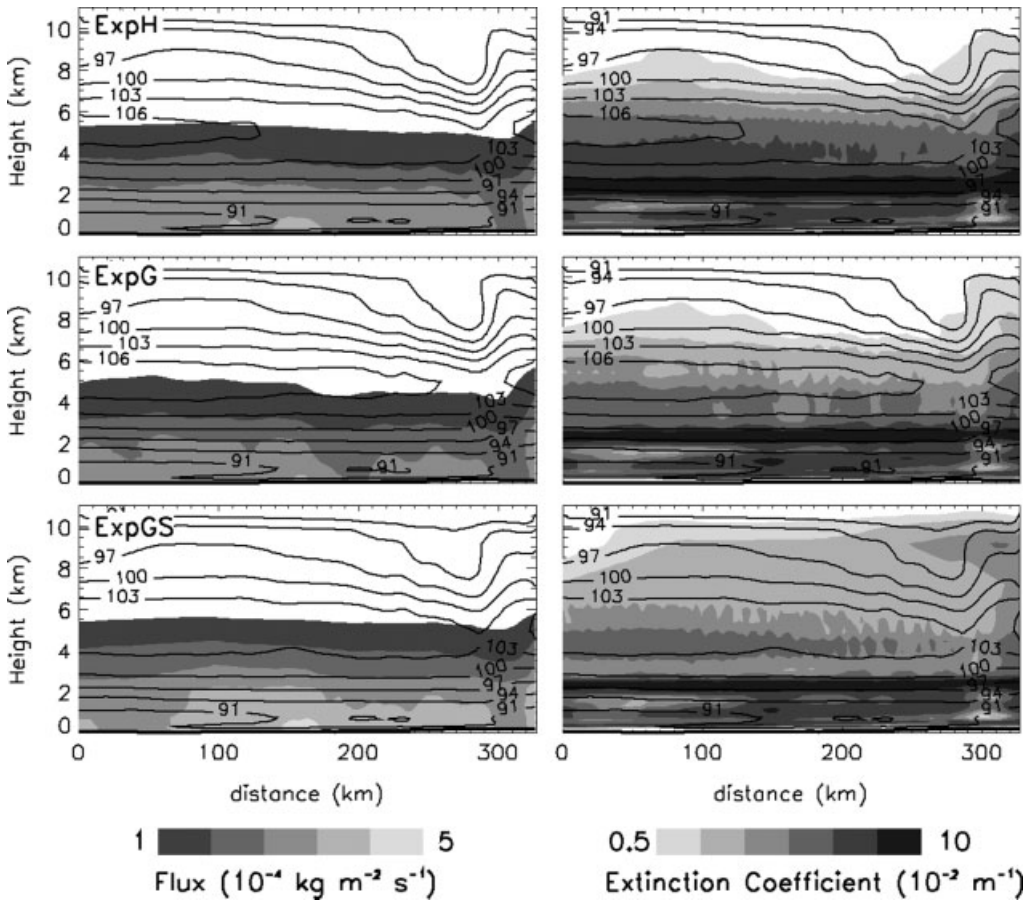

Figure 12. Vertical cross-sections for a stratiform case on 5 October 2008 at 0800 UTC. Average vertical cross-sections of (left) precipitation rates (all hydrometeor species) and (right) visible extinction coefficient for (top) ExpH, (middle) ExpG, and (bottom) ExpGS. Cross-sections were taken along the mean wind vector at 500 hPa and the figure shows an average for those cross-sections having average precipitation rates above 10^{-5} kg m^{-2} s^{-1} near the surface. Black contours denote the relative humidity with respect to ice (%).

too vigorous when they are forced on coarser-than-natural scales. Bryan and Morrison (2012) suggested that entrainment rates in updraughts become larger when horizontal resolution decreases. Therefore, some of the sensitivities presented here might be resolution-dependent to some extent. The reasons for differences in domain-maximum precipitation accumulations among the different experiments are explored in section 3.3.2.

3.3. Detailed analysis of selected cases

In order to obtain more insight into the reasons for the sensitivities between the different experiments discussed in the previous sections, a more detailed analysis was performed of one stratiform and one convective case that were representative of their respective composite.

3.3.1. Stratiform case: 5 October 2008

On 5 October 2008 an active cold front, associated with a deep surface depression tracking from Scotland to Scandinavia, lingered for many hours over much of northwestern Europe. During the same period, a fast-moving short-wave trough at 500 hPa triggered a rapidly deepening wave on this cold front leading to intensification during the afternoon hours. Precipitation accumulations over 24 hours on this day ranged from 10 to 40 mm in Belgium. As far as the model sensitivities are concerned, this case behaved in a typical way for the entire stratiform composite. Compared to ExpH, surface precipitation is slightly reduced in ExpG and slightly enhanced in ExpGS. Cloud optical thickness is reduced in ExpG and ExpGS compared to ExpH and cloud-top pressure is most reduced by ExpGS.

Figure 12 shows vertical cross-sections of precipitation rate and cloud optical thickness for each of the experiments on 5 October 2008 at 0800 UTC. Note that very similar cross-sections were found for most other cases in the composite (not shown). The precipitation fluxes and cloud-top heights (pressures) are similar in ExpH and ExpG, despite somewhat optically thinner clouds in ExpG. A more dramatic impact occurs in ExpGS, however, showing enhanced near-surface precipitation rates and significantly more elevated cloud tops. Figure 12 also shows the relative humidity with respect to ice within clouds and, from this figure, in-cloud ice supersaturation is clearly lower in ExpGS than in ExpG and ExpH (as indicated by the absence of the ‘ 106’ contours). Most likely, this can be attributed to enhanced depositional growth of snow, as outlined in section 3.1. Figure 13 shows vertical profiles of several snow characteristics for the three experiments. Due to the temperature-dependent N_{0S} in ExpGS, the diameters of snowflakes aloft are much smaller (Figure 13(c)) and are at least an order of magnitude more numerous (Figure 13(b)) than for the other experiments. Hence, the effective surface area of snowflakes to take up excess water vapour is increased. Moreover, snowflakes not only are smaller in ExpGS, but fall more slowly

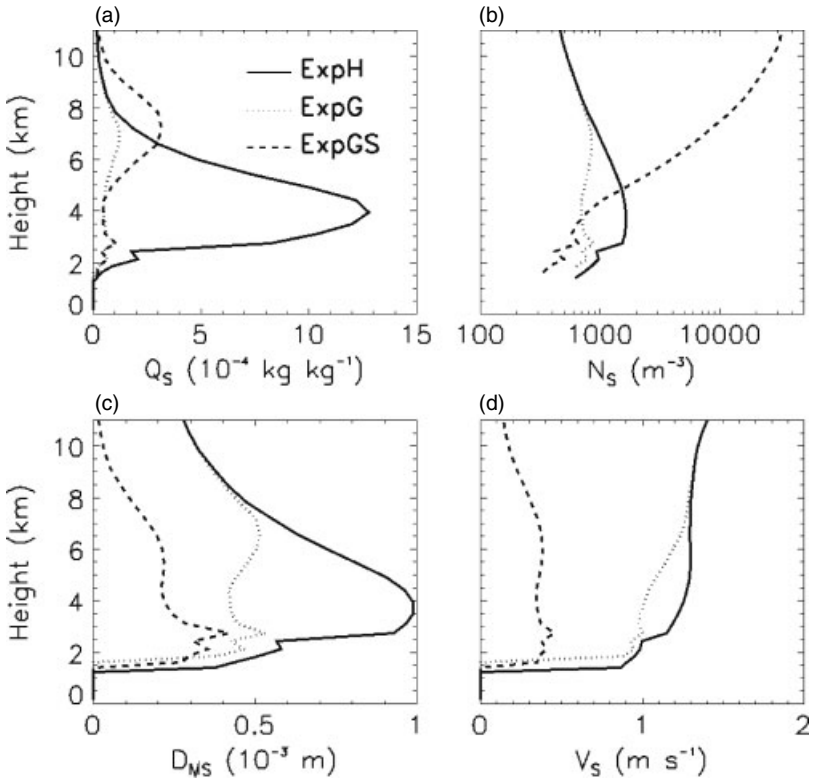

Figure 13. Domain-averaged vertical profiles of snow characteristics on 5 October 2008 at 0800 UTC for all experiments: (a) mixing ratio, (b) number concentration, (c) mass-weighted mean diameter, and (d) bulk terminal vertical velocity.

Table 6. Domain- and time-averaged COT (transmission-averaged COT), time-averaged CTP for cloudy grid cells, and 24-hour accumulated domain-averaged (domain-maximum) surface precipitation as observed on 5 October 2008 and 5 May 2006 and as simulated by each of the experiments.

COT	Observed	ExpH	ExpG	ExpGS
5 October 2008	57.1 (2.2)	35.7 (1.5)	28.2 (1.4)	27.1 (1.7)
5 May 2006	4.4 (0.4)	1.7 (0.5)	1.6 (0.5)	2.1 (0.7)
CTP				
5 October 2008 (hPa)	368.5	413.0	423.9	364.4
5 May 2006 (hPa)	356.0	564.4	577.7	430.0
Surface Precipitation				
5 October 2008 (mm)	10.5 (43.7)	15.8 (59.6)	14.9 (59.5)	17.0 (59.5)
5 May 2006 (mm)	2.3 (70.4)	2.7 (123.0)	2.8 (87.8)	2.9 (58.6)

(Figure 13(d)). Above 5000 m altitude, snow fall speeds on average are about 4–5 times smaller in ExpGS as compared to the other experiments (Figure 13(d)). In fact, the sizes of snow aloft in ExpGS are more typical of small ice crystals. These small snowflakes hence remain suspended aloft and gradually sublimate, rather than falling towards the surface as in ExpG and ExpH. Due to the suspension of snow aloft as well as the additional cooling due to its sublimation, cloud tops are elevated, which is a clear model improvement compared to observations (Table 6).

At mid-levels, the more efficient removal of excess water vapour by snow depositional growth in ExpGS reduces the supersaturation with respect to ice (Figure 12). The presence of large numbers of small graupel particles at these levels in ExpG and ExpGS (not shown) prevents the snow mixing ratios from growing larger as for ExpH (Figure 13(b)), as most of the snow is collected by graupel. From the higher precipitation rates in Figure 12, the more efficient removal of excess water vapour in ExpGS also likely enhances precipitation efficiency and hence surface precipitation. Woods *et al.* (2007) found a similar impact of lower relative humidity with respect to ice and enhanced surface precipitation in a cold front simulation, when using non-spherical instead of spherical snowflakes. Similar to our findings for a broad range of stratiform cases, Colle *et al.* (2005) also found a 10 to 15% increase in surface precipitation for frontal stratiform simulations when a temperature-dependent N_{0S} was applied as compared to using a fixed N_{0S}.

3.3.2. *Convective case: 5 May 2006*

On 5 May 2006, slightly unstable air masses were advected over Belgium along the western flank of an extensive, but weakening ridge across central Europe. A region of enhanced mid-level moisture led to somewhat increased convective available potential energy (CAPE) values of up to 100–300 J kg^{-1} during the afternoon over northeastern France, southeastern Belgium and western Germany. Strong convective forcing was missing, but isolated thunderstorms developed above higher terrain of the Ardennes region in southern Belgium. Despite the weak forcing and modest

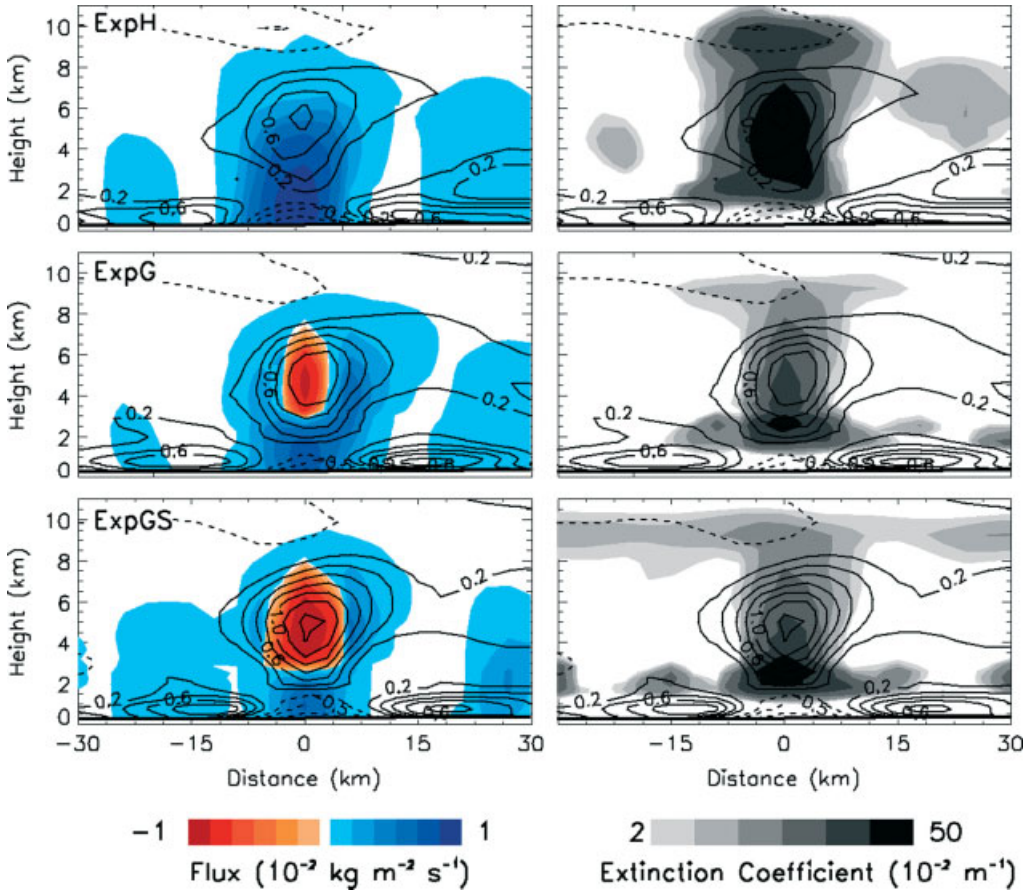

Figure 14. Vertical cross-sections for convective case on 5 May 2006 at 1600 UTC. Average vertical cross-sections of (left) precipitation rates (all hydrometeor species) and (right) extinction coefficient, for (top) ExpH, (middle) ExpG and (bottom) ExpGS. Cross-sections were taken along the mean wind vector at 500 hPa and the figure shows an average for the 15 cross-sections having the strongest updraught at 500 hPa. All cross-sections were centred at the location of the strongest updraught before averaging was applied. Red shading in the left panels denotes upward precipitation fluxes, while blue shading denotes downward fluxes. Black contours denote the perturbation potential temperature (in K), defined as the deviation of potential temperature from the mean potential temperature at each level. Solid contours are positive and dashed lines are negative temperature perturbations.

instability, accumulations up to 50 mm over a few hours were reported locally, due to the lack of strong horizontal flow or vertical wind shear.

The location and timing of the thunderstorms was well captured by all three model experiments. This case is representative for the entire convective composite, as ExpG and ExpH behave similarly in terms of cloud properties (Table 6), although the maximum-accumulated surface precipitation is reduced in ExpG. ExpGS further reduces the maximum-accumulated surface precipitation, and CTP is more elevated and hence closer to the observations in ExpGS compared to ExpG and ExpH. Figure 14 shows vertical cross-sections of precipitation rate and extinction coefficient along the mean wind vector on 5 May 2006 at 1600 UTC, when storms were mature. The larger fraction of high clouds in ExpGS is clearly associated with more extensive anvil clouds attached to the thunderstorms as compared to the ExpH and ExpG. These anvils entirely consist of snow (not shown). Snow fall speeds at these high altitudes (and hence low temperatures) are very low as their number concentration becomes very high. While snow falls to the surface very quickly after it is produced in ExpH and ExpG, it resides aloft for a much longer time in ExpGS and is more easily transported by the upper-level divergent flows away from the updraught regions. At these levels, snow is gradually lost by sublimation into the surrounding dry air, rather than falling out to the surface. From Figure 14, precipitation rates in the experiments containing graupel instead of hail are significantly lower. Due to the slow fall speed of graupel, the direction of the average precipitation flux is even reversed (and hence upward) in the main updraught regions. Freezing processes associated with these large graupel amounts (leading to more glaciation and less cloud water, see Figure 5(b)) lead to more latent heat release within updraughts, as suggested by the contours on Figure 14. As precipitation efficiency is also lower, as mentioned in section 3.2 and by e.g. Van Weverberg *et al.* (2011), domain-average precipitation is not affected much. To understand better why domain-maximum precipitation is reduced so much in the experiment containing graupel, Figure 15 (like Figure 12(d) and (e)) shows vertical profiles of precipitation flux. However, while Figure 12 represents a domain average for the stratiform case, Figure 15 shows the vertical profile for grid cells with the most intense surface precipitation rates (precipitation rates in excess of 20 mm h^{-1}). While on the average across the domain, the downward fluxes of graupel in ExpG and ExpGS are comparable to those of hail in ExpH, this is not the case for grid cells within the most intense surface precipitation. Strong updraughts associated with the most intense surface precipitation indeed hinder the fallout of the slowly falling graupel particles and even reverse the downward flux at certain levels. Hail falls about 10 times faster than graupel and hence its downward flux is affected little by such updraughts. As graupel falls out even

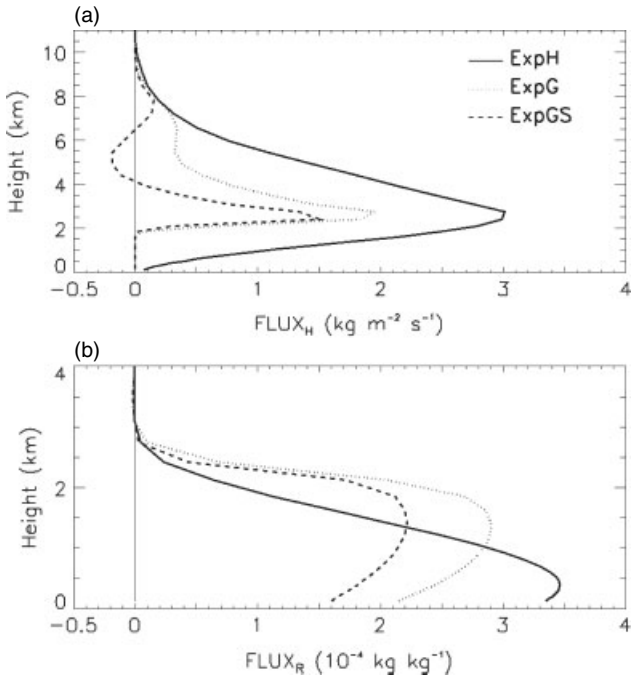

Figure 15. Vertical profiles of (a) graupel or hail mass flux, and (b) rain mass flux, associated with grid cells experiencing surface rain rates in excess of 20 mm h^{-1} for the three experiments. Positive fluxes are downward and negative fluxes are upward.

slower in ExpGS than in ExpG, maximum precipitation rates are even further reduced.

4. Conclusions

The sensitivity of simulated clouds and surface precipitation to size distribution assumptions of the precipitating hydrometeors in a one-moment bulk microphysics scheme has been investigated for 15 convective and 15 stratiform intense precipitation events observed in a coastal midlatitude region (Belgium). Furthermore, we have performed an extensive verification against satellite-retrieved cloud properties and radar–rain-gauge retrieved surface precipitation.

We have shown that the inclusion of graupel as opposed to hail as the largest rimed ice species in the microphysics parametrization strongly impacted the vertical profiles of snow and graupel content. However, because snow and graupel sizes are much larger than cloud drops and ice crystals, there was no clear impact on the cloud optical thickness distribution. Generally, the fraction of thin clouds of the total cloudy area was overestimated. The total cloudy area was itself underestimated, however, so that transmission-averaged cloud optical thickness was underestimated and too much radiation would reach the surface in most cases. The latter was mainly an issue in the convective composite. Cloud-top pressure distribution was significantly improved by introducing non-spherical snow particles and a temperature-dependent intercept parameter, which caused larger depositional growth rates of snow at high altitudes. Clouds that included graupel and modified snow size distributions during convective and stratiform events yielded classifications that consistently agreed better with satellite observations. Hence, we confirm and generalize (even for convective clouds) prior findings (e.g. Thompson *et al.*, 2004; Colle *et al.*, 2005; Woods *et al.*, 2007) that increased snow depositional growth at low temperatures and hence deeper clouds are obtained using more realistic snow size distributions. Although we found this to be a clear model improvement, we cannot be certain that this result is obtained for the right reasons. Aircraft campaigns such as the Improvement of Microphysical Parameterization through Observational Verification Experiment (IMPROVE: Stoelinga *et al.*, 2003) are required to identify whether the vertical distributions of hydrometeors are also better represented in the improved model versions.

The inclusion of graupel as opposed to hail did not significantly affect surface precipitation during virtually any of our stratiform or convective simulations, in contrast to many previous idealized studies (Gilmore *et al.*, 2004; van den Heever and Cotton, 2004; Morrison and Milbrandt, 2011). Only domain-maximum precipitation was modestly affected in most of the convective events, with generally lower values for experiments containing graupel. We demonstrated that the magnitude of the sensitivity to the choice of the rimed ice species in our simulations correlated well with several environmental variables, such as updraught speed and the freezing-level height. Part of the explanation for the difference between our real-case simulations and previous idealized simulations might be that none of our experiments had similar updraught velocities or similarly high freezing levels as in the idealized experiments, which were associated with very strong, deep convective systems. Such storm systems are atypical for western Europe and most intense precipitation events are associated with less deep and less vigorous convection. Hence, it would be worthwhile to conduct a series of idealized experiments with colder boundary layers and less vigorous storm systems to gain understanding into the role that these aspects play in the sensitivity of surface precipitation to the choice of the rimed ice species. As documented before (e.g. Colle *et al.*, 2005; Woods *et al.*, 2007), improved snow size distributions tend to enhance precipitation during coastal midlatitude stratiform precipitation events, due to more-efficient removal of supersaturation with respect to ice at high altitudes. This behaviour was not found here during convective events, however.

It should be stressed that this research was conducted for a one-moment bulk microphysics scheme, while two-moment microphysics schemes have recently become available for NWP applications. However, it has been shown by Morrison and Milbrandt (2011) that the choice of graupel vs. hail is an issue for two-moment microphysics schemes as well. Two-moment microphysics schemes do not suffer from issues associated with using constant intercept parameters of the precipitation size distributions. However, we showed that a diagnostic treatment of the snow intercept parameter could to some extent reproduce the behaviour reported in simulations using two-moment schemes (Milbrandt *et al.*, 2010). It should be further investigated how one-moment schemes with diagnostic intercept parameters (which are more computationally efficient) compare with two-moment schemes.

Acknowledgements

This research was carried out in the framework of the QUEST-B project, funded by the Flemish Fund for Scientific Research (FWO-Vlaanderen). We would like to

acknowledge the Center for Analysis and Prediction of Storms (CAPS) of Oklahoma University for providing the ARPS source code online, and the Deutscher Wetterdienst (DWD) for providing the Satellite Application Facility on Climate Monitoring (CM-SAF) satellite-derived cloud properties. We are also grateful to the European Environment Agency for making available the CORINE land cover data, the US Geological Survey for the GTOPO30 terrain-height dataset, the Deutsches Zentrum für Luft- und Raumfahrt (DLR) for the processed AVHRR imagery for sea-surface temperature, and the Flemish Institute for Technological Research (VITO) for the SPOT vegetation NDVI imagery. This research is conducted utilising high-performance computational resources provided by the Earth System Modeling Program via the FASTER-project (http://www.bnl.gov/esm) and the University of Leuven (http://ludit.kuleuven.be/hpc). Additional support for this project was provided by the US Department of Energy's Atmospheric Science Program Atmospheric System Research, an Office of Science Office of Biological and Environmental Research program, under contract DE-AC02-98CH10886, and the Climate System Modeling (ESM) via the FASTER project.

References

Akkermans T, Böhme T, Demuzere M, Crewell S, Selbach C, Reinhardt T, Seifert A, Ament F, van Lipzig NPM. 2012. Regime-dependent evaluation of accumulated precipitation in COSMO. *Theor. Appl. Climatol.*, DOI: 10.1007/s00704-011-0502-0 (in press).

Böhme T, Stapelberg S, Akkermans T, Crewell S, Fischer J, Reinhardt T, Seifert A, Selbach C, van Lipzig NPM. 2011. Long-term evaluation of COSMO forecasting using combined observational data of the GOP period. *Meteorol. Z.* **20**: 119–132.

Bryan GH, Morrison H. 2012. Sensitivity of a simulated squall line to horizontal resolution and parameterization of microphysics. *Mon. Weather Rev.* **140**: 202–225.

Bryan GH, Wyngaard JC, Fritsch JM. 2003. Resolution requirements for the simulation of deep moist convection. *Mon. Weather Rev.* **131**: 2394–2416.

Bugliaro L, Zinner T, Keil C, Mayer B, Hollmann R, Reuter M, Thomas W. 2010. Validation of cloud property retrievals with simulated satellite radiances: A case study for SEVIRI. *Atmos. Chem. Phys. Discuss.* **10**: 21931–21988.

Cohen C, McCaul Jr EW. 2006. The sensitivity of simulated convective storms to variations in prescribed single-moment microphysics parameters that describe particle distributions, sizes, and numbers. *Mon. Weather Rev.* **134**: 2547–2565.

Colle BA, Garvert MF, Wolfe JB, Mass CF, Woods CP. 2005. The 13–14 December 2001 IMPROVE-2 event. Part III: Simulated microphysical budgets and sensitivity studies. *J. Atmos. Sci.* **62**: 3535–3558.

Cox GP. 1988. Modelling precipitation in frontal rainbands. *Q. J. R. Meteorol. Soc.* **114**: 115–127.

Crewell S, Mech M, Reinhardt T, Selbach C, Betz H-D, Brocard E, Dick G, O'Connor E, Fischer J, Hanisch T, Hauf T, Hünerbein A, Delobbe L, Mathes A, Peters G, Wernli H, Wiegner M, Wulfmeyer V. 2008. The general observation period 2007 within the priority program on quantitative precipitation forecasting: Concept and first results. *Meteorol. Z.* **17**: 849–866.

Deng AJ, Stauffer DR. 2006. On improving 4-km mesoscale model simulations. *J. Appl. Meteorol. Clim.* **45**: 361–381.

Federer B, Waldvogel A. 1975. Hail and raindrop size distributions from a Swiss multicell storm. *J. Appl. Meteorol.* **14**: 91–97.

Ferrier BS. 1994. A double-moment multiple-phase four-class bulk ice scheme. Part I: Description. *J. Atmos. Sci.* **51**: 249–280.

Fu Q, Liou KN. 1993. Parameterization of the radiative properties of cirrus clouds. *J. Atmos. Sci.* **50**: 2008–2025.

Gilmore MS, Straka JM, Rasmussen EN. 2004. Precipitation uncertainty due to variations in precipitation particle parameters within a simple microphysics scheme. *Mon. Weather Rev.* **132**: 2610–2627.

Goudenhoofdt E, Delobbe L. 2009. Evaluation of radar–gauge merging methods for quantitative precipitation estimates. *Hydrol. Earth Syst. Sci.* **13**: 195–203.

Gunn KLS, Marshall JS. 1958. The distribution with size of aggregate snowflakes. *J. Meteorol.* **15**: 452–461.

Houze Jr RA, Hobbs PV, Herzegh PH, Parsons DB. 1979. Size distributions of precipitation particles in frontal clouds. *J. Atmos. Sci.* **36**: 156–162.

Jakob C. 2003. An improved strategy for the evaluation of cloud parameterizations in GCMs. *Bull. Am. Meteorol. Soc.* **84**: 1387–1401.

Kain JS, Fritsch JM. 1993. Convective parameterization for mesoscale models: The Kain–Fritsch scheme. The Representation of Cumulus Convection in Numerical Models. *Meteorol. Monogr.* **24**: 165–170.

Karlsson K-G, Willén U, Jones C, Wyser K. 2008. Evaluation of regional cloud climate simulations over Scandinavia using a 10-year NOAA Advanced Very High Resolution Radiometer cloud climatology. *J. Geophys. Res.* **113**: D01203, DOI: 10.1029/2007JD008658.

Keil C, Tafferner A, Mannstein H, Schättler U. 2003. Evaluating high-resolution model forecasts of European winter storms by use of satellite and radar observations. *Weather and Forecasting* **18**: 732–747.

Kong FY, Yau MK. 1997. An explicit approach to microphysics in MC2. *Atmos.–Ocean* **35**: 257–291.

Lin Y-L, Farley RD, Orville HD. 1983. Bulk parameterization of the snow field in a cloud model. *J. Clim. Appl. Meteorol.* **22**: 1065–1092.

Liu JY, Orville HD. 1969. Numerical modeling of precipitation and cloud shadow effects on mountain-induced cumuli. *J. Atmos. Sci.* **26**: 1283–1298.

Locatelli JD, Hobbs PV. 1974. Fall speeds and masses of solid precipitation particles. *J. Geophys. Res.* **79**: 2185–2197.

Luo ZJ, Liu GY, Stephens GL. 2010. Use of A-Train data to estimate convective buoyancy and entrainment rate. *Geophys. Res. Lett.* **37**: L09804, DOI: 10.1029/2010GL042904.

Marshall JS, Palmer WM. 1948. The distribution of raindrops with size. *J. Meteorol.* **5**: 165–166.

Milbrandt JA, Yau MK. 2005. A multimoment bulk microphysics parameterization. Part II: A proposed three-moment closure and scheme description. *J. Atmos. Sci.* **62**: 3065–3081.

Milbrandt JA, Yau MK, Mailhot J, Bélair S, McTaggert-Cowan R. 2010. Simulation of an orographic precipitation event during IMPROVE-2. Part II: Sensitivity to the number of moments in the bulk microphysics scheme. *Mon. Weather Rev.* **138**: 625–642.

Morrison H, Milbrandt JA. 2011. Comparison of two-moment bulk microphysics schemes in idealized supercell thunderstorm simulations. *Mon. Weather Rev.* **139**: 1103–1130.

Morrison H, Curry JA, Khvorostyanov VI. 2005. A new double-moment microphysics parameterization for application in cloud and climate models. Part I: Description. *J. Atmos. Sci.* **62**: 1665–1677.

Noilhan J, Planton S. 1989. A simple parameterization of land surface processes for meteorological models. *Mon. Weather Rev.* **117**: 536–549.

Otkin JA, Greenwald TJ. 2008. Comparison of WRF model-simulated and MODIS-derived cloud data. *Mon. Weather Rev.* **136**: 1957–1970.

Reinhardt T, Seifert A. 2006. A three-category ice scheme for LMK. *Cosmo Newsletter* **6**: 115–120, http://www.cosmo-model.org

Roebeling RA, Feijt AJ, Stammes P. 2006. Cloud property retrievals for climate monitoring: Implications of differences between Spinning Enhanced Visible and Infrared Imager (SEVIRI) on METEOSAT-8 and Advanced Very High Resolution Radiometer (AVHRR) on NOAA-17. *J. Geophys. Res.* **111**: D20210, DOI: 10.1029/2005JD006990.

Rossow WB, Schiffer RA. 2001. Advances in understanding clouds from ISCCP. *Bull. Am. Meteorol. Soc.* **80**: 2261–2287.

Rutledge SA, Hobbs PV. 1983. The mesoscale and microscale structure and organization of clouds and precipitation in midlatitude cyclones. VIII: A model for the 'seeder–feeder' process in warm-frontal rainbands. *J. Atmos. Sci.* **40**: 1185–1206.

Schröder M, van Lipzig NPM, Ament F, Chaboureau J-P, Crewell S, Fischer J, Matthias V, van Meijgaard E, Walther A, Willén U. 2006. Model predicted low-level cloud parameters. Part II: Comparison with satellite remote sensing observations during the BALTEX Bridge Campaigns. *Atmos. Res.* **82**: 83–101.

Schulz J, Thomas W, Müller R, Behr H-D, Caprion D, Deneke H, Dewitte S, Dürr B, Fuchs P, Gratzki A, Hechler P, Hollmann R, Johnston S, Karlsson K-G, Manninen T, Reuter M, Riihelä A, Roebeling R, Selbach N, Tetzlaff A, Wolters E, Zelenka A, Werscheck M. 2009. Operational climate monitoring from space: The EUMETSAT Satellite Application Facility on Climate Monitoring (CM-SAF). *Atmos. Chem. Phys.* **9**: 1687–1709.

Seifert A, Beheng KD. 2006. A two-moment cloud microphysics parameterization for mixed-phase clouds. Part 2: Maritime vs. continental deep convective storms. *Meteorol. Atmos. Phys.* **92**: 67–82.

Serafin S, Ferretti R. 2007. Sensitivity of a mesoscale model to microphysical parameterizations in the MAP SOP events IOP2b and IOP8. *J. Appl. Meteorol. Clim.* **46**: 1438–1454.

Stoelinga MT, Hobbs PV, Mass CF, Locatelli JD, Colle BA, Houze Jr RA, Rangno AL, Bond NA, Smull BF, Rasmussen RM, Thompson G, Colman BR. 2003. Improvement of microphysical parameterization through observational verification experiment. *Bull. Am. Meteorol. Soc.* **84**: 1807–1826.

Sui C-H, Li X, Lau K-M. 1998. Radiative–convective processes in simulated diurnal variations of tropical oceanic convection. *J. Atmos. Sci.* **55**: 2345–2357.

Sun W-Y, Chang C-Z. 1986. Diffusion model for a convective layer. Part I: Numerical simulation of convective boundary layer. *J. Clim. Appl. Meteorol.* **25**: 1445–1453.

Tao W-K, Simpson J, Baker D, Braun S, Chou M-D, Ferrier B, Johnson D, Khain A, Lang S, Lynn B, Shie C-L, Starr D, Sui C-H, Wang Y, Wetzel P. 2003. Microphysics, radiation and surface processes in the Goddard Cumulus Ensemble (GCE) model. *Meteorol. Atmos. Phys.* **82**: 97–137.

Thompson G, Rasmussen RM, Manning K. 2004. Explicit forecasts of winter precipitation using an improved bulk microphysics scheme. Part I: Description and sensitivity analysis. *Mon. Weather Rev.* **132**: 519–542.

van den Heever SC, Cotton WR. 2004. The impact of hail size on simulated supercell storms. *J. Atmos. Sci.* **61**: 1596–1609.

van Lipzig NPM, Schröder M, Crewell S, Ament F, Chaboureau J-P, Löhnert U, Matthias V, van Meijgaard E, Quante M, Willén U, Wen WC. 2006. Model predicted low-level cloud parameters. Part I: Comparison with observations from the BALTEX Bridge Campaigns. *Atmos. Res.* **82**: 55–82.

Van Weverberg K, van Lipzig NPM, Delobbe L. 2011a. The evaluation of moist processes in km-scale NWP models using remote sensing and *in situ* data: Impact of size distribution assumptions. *Atmos. Res.* **99**: 15–38.

Van Weverberg K, van Lipzig NPM, Delobbe L. 2011b. The impact of size distribution assumptions in a bulk one-moment microphysics scheme on simulated surface precipitation and storm dynamics during a low-topped supercell case in Belgium. *Mon. Weather Rev.* **139**: 1131–1147.

Van Weverberg K, Vogelmann AM, Morrison H, Milbrandt JA. 2012. Sensitivity of idealized squall line simulations to the level of complexity used in two-moment bulk microphysics schemes. *Mon. Weather Rev.*, in press, DOI: 10.1175/MWR-D-11-00120.1.

Wisner C, Orville HD, Myers C. 1972. A numerical model of a hail-bearing cloud. *J. Atmos. Sci.* **29**: 1160–1181.

Woods CP, Stoelinga MT, Locatelli JD. 2007. The IMPROVE-1 storm of 1–2 February 2001. Part III: Sensitivity of a mesoscale model simulation to the representation of snow particle types and testing of a bulk microphysical scheme with snow habit prediction. *J. Atmos. Sci.* **64**: 3927–3948.

Xue M. 2000. High-order monotonic numerical diffusion and smoothing. *Mon. Weather Rev.* **128**: 2853–2864.

Xue M, Droegemeier KK, Wong V. 2000. The Advanced Regional Prediction System (ARPS) – A multi-scale nonhydrostatic atmospheric simulation and prediction model. Part I: Model dynamics and verification. *Meteorol. Atmos. Phys.* **75**: 161–193.

Xue M, Droegemeier KK, Wong V, Shapiro A, Brewster K, Carr F, Weber D, Liu Y, Wang D. 2001. The Advanced Regional Prediction System (ARPS) – A multi-scale nonhydrostatic atmospheric simulation and prediction tool. Part II: Model physics and applications. *Meteorol. Atmos. Phys.* **76**: 143–165.

